DEVELOPMENT OF ELECTROHYDRODYNAMIC (EHD) LIQUID MICROPUMPS FOR ELECTRONICS COOLING APPLICATIONS

MASTER THESIS (2007) MCMASTER UNIVERSITY

(Mechanical Engineering) Hamilton, Ontario, Canada

TITLE: Development of Electrohydrodynamic
(EHD) Liquid Micropumps for Cooling
Applications.

AUTHOR: Pouya Zangeneh Kazemi, B.Eng.

SUPERVISORS: Dr. C.Y. Ching and Dr. P. Selvaganapathy

NUMBER OF PAGES: xiv, 99

ABSTRACT

Emergence of efficient cooling techniques has been a crucial factor in development of faster and more powerful electronic equipment and ICs. One of the key obstacles towards further miniaturization is efficient heat removal from regions of high temperature to maintain continued operation of these devices below their maximum operating range. Recently, a significant amount of research has been directed to develop liquid based cooling techniques. For example, microchannel heat-sinks have been designed to remove up to 1 kW/cm^2. Developing microscale actuators that provide sufficient pressure head is essential for integrating these microscale cooling schemes with the electronic devices. Different techniques can be used to pump fluid in the microscale such as electroosmotic, magnetohydrodynamic, and electrohydrodynamic (EHD) pumping. Among these technologies, EHD pumps are particularly promising for microfluidic devices because they use no moving parts, and uses very small power and has low cost and maintenance requirements.

This work presents the development and test of EHD micropumps with different electrode configurations. Four different electrode configurations: (1) planar symmetric electrodes, (2) planar asymmetric electrodes, (3) 3-D symmetric electrodes, and (4) 3-D asymmetric electrodes were investigated. In addition, the effect of different design specifications, such as the inter-electrode spacing and spanwise spacing of the micropillars were investigated. The electrodes were fabricated using a two mask process. First, a thin layer of chromium was deposited on glass as a seed layer for gold electrodes. Positive photoresist (AZ P4620) was

patterned to form the mould for the micropillar electrodes. Nickel was electroplated to fill the mold. Subsequently, a Cr/Au layer was patterned to devise the electrode base connector and pads. The microfluidic channels were fabricated by casting polydimethylsiloxane (PDMS) on top of an SU-8 100 (MicroChem Corp.) mould which was patterned to delineate the microchannel structure. The PDMS microchannel was integrated on the electrode base by plasma oxidizing the PDMS and glass wafer, and sealing the connection with liquid PDMS.

The pump performance was experimentally determined with Methoxynonafluorobutane (HFE-7100) as the working fluid. All of the micropumps were tested under a no net flow condition to find the maximum pressure generation. The micropumps with planar and asymmetric planar electrode configurations were also tested for maximum flow rate under no imposed back pressure. The results show that the micropumps with the 3D asymmetric electrode design generated a higher pressure head compared to the other micropumps with identical inter electrode spacing under no flow conditions. The micropumps with planar asymmetric design had a higher performance compared to the micropumps with planar asymmetric electric under both no flow condition and no back pressure condition. A maximum pressure head of 2240 Pa was generated at an applied voltage of 900 V by the micropump with 3D asymmetric electrode design. A maximum flow rate of 0.127 mL/min was achieved by the micropump with planar asymmetric electrode configurations. This is five times higher than the maximum flow rate generated by the micropump with the planar symmetric electrode design.

DEDICATED

TO

AZADEH

ACKNOWLEDGMENTS

First and foremost I would like to express my gratitude to both my supervisors, Dr. C.Y. Ching and Dr. P. Selvaganapathy, for the guidance that they provided to me. I will be always grateful for the unique opportunity that you offered me and for the faith and trust that you put in me.

I would also like to thank CEDT research staff, Doris Stevanovic, Graham Pearson, Dr. Z. Peng, and Dr. D. Bruce, who have been graciously supportive and helpful. Without your expert advice, I would not be able to overcome all the challenges that I faced. I would also thank Joe Verhaeghe, who helped me with the electrical aspects of the thesis.

In the course of last two years in McMaster University, I made a lot of good friends, which makes this experience even more cherishable for me. They also helped me with my thesis. I want to thank all of them specially Bala, Simon, Arash, Geetha, Hossam, Jared, Sarvesh, and Wen.

I want to express my appreciation to my parents, Mohammad and Tooba. Your endless support and love made this accomplishment possible.

Finally, to my wife, without your support and love this could not have been possible. I gratefully appreciate your patience and understanding during last two years. You motivated me and inspired me and for that I thank you.

TABLE OF CONTENTS

Chapter 4: Experimental Results & Discussion

Chapter 5: Conclusion and Recommendations for Future Works

LIST OF FIGURES

LIST OF TABLES

Chapter 1: Introduction

There is an increasing trend in microelectronics towards smaller size and high density transistors, which increases the local power density of these devices. One of the key obstacles towards further miniaturization is efficient heat removal from these devices to maintain the temperature below their maximum operating range. Thus, there has been a significant effort to develop efficient cooling techniques, which is a crucial factor in further development of faster and more powerful electronic equipments and ICs. The traditional conventional air-based cooling technologies are unable to achieve the high heat flux density rates of emerging microscale electronic systems. Hence, there is a need for more innovative liquid based microscale cooling technologies. Since the advent of microfabrication techniques, a significant amount of research has been

devoted to developing microchannel heat sinks. For example, microchannel heat sinks have been developed that can remove more than $1kW/cm^2$ of heat dissipation (Jiang et al. 2001). A key component of any microscale cooling system is the microscale actuator or micropump that can provide sufficient pressure head for the required flow rates.

Micropumps are an essential component of many microfluidic systems such as micromixers, chemical analysis systems, and microdosing systems with biomedical and medical applications. Micropumps can be categorized in four different groups:

i.   Mechanical micropumps (e.g. vibrating diaphragm micropumps) (Van Lintel et al. 1998).

ii. Electrokinetic and magnetokinetic micropumps (e.g. electrohydrodynamic (EHD) pumps). (Jang et. Al 2000)

iii. Phase change micropumps (e.g. bubble pumps). (Lee and Kim 2000)

iv. Novel micropumps (e.g. electrowetting micropumps). (Jun et al. 1996)

The focus of the present study was to research and develop a reliable and effective micropump. Among the different micropump mechanisms available, an EHD pump was chosen because of its applicability to microelectronics cooling as well as to an array of biomedical applications and other local microfluidic applications. EHD pumping has many advantages: (a) it is relatively simple to implement in small-scale structures using standard microfabrication techniques, (b) it does not have any mechanically wearable parts, and thus cause no significant acoustic signature due to vibration, (c) it is easily controllable since input electric power is directly related to the flow rate in a particular device, and (d) it consumes little power and is attractive not

only in conventional electronics, but also in the fast-growing mobile and portable electronics industries.

1.1 Research objectives

The present work aims to develop, manufacture and characterize EHD pumping techniques for microscale cooling applications. The feasibility of an EHD micropump was determined and the effect of the main design features on the pumping performance was characterized. The specific objectives are:

i. To investigate the effect of novel electrode configurations on EHD micropumps and determine methods to improve the performance of EHD pumping. Four different planar and 3-D electrode configurations were developed and evaluated.

ii. To investigate the effect of inter-electrode spacing on the performance of EHD micropumps with different electrode configurations.

iii. To investigate the effect of micropillar distance in span wise direction on EHD pumps with 3-D electrode configurations.

1.2 Scope

This thesis consists on five chapters, including this introduction chapter. Fundamentals of EHD pumping mechanisms and the basic governing equations are presented in Chapter 2. A literature review of the existing work in the field is also presented in this chapter. The design and fabrication process of the EHD micropumps with different novel electrode designs are presented in Chapter 3. The experimental results of these micropumps are presented and discussed in Chapter 4. Finally, Chapter 5 provides an overview and conclusions from this study. The experimental results from different designs and the key conclusions are presented.

Chapter 2: Fundamentals of Electro-hydrodynamic Pumping Mechanisms

2.1 Introduction

In electrohydrodynamics (EHD), forces are exerted on free or polarized charges in a fluid medium by means of an imposed electric field, which can set the fluid into motion under certain conditions. The movement of these charges modifies the electric field which results in a two-way interaction between the fluid flow and electrostatics, making electrohydrodynamic a complex physical phenomenon. This two way interaction has been investigated for many different applications, including EHD pumping which is the focus of this investigation. There are different EHD pumping mechanisms based on the different means by which charges are established in the dielectric fluid medium. In this chapter, these EHD pumping mechanisms are reviewed with an emphasis on ion drag EHD pumps. Subsequently, the fundamental physics of EHD phenomenon and its governing equations are presented. Finally, a literature review of existing research in the field is presented.

2.2 EHD pumping mechanisms

A number of micropumps have been developed in the recent past for microelectronics cooling applications. These include vibrating diaphragm pumps (Van Lintel et al. 1998), magnetohydrodynamic pumps (MHD) (Jang and Lee 2000), and electrohydrodynamic (EHD) pumps (Richter et al. 1991). Amongst these technologies, EHD pumps are particularly promising for microfluidic devices because they have no moving parts, consume very small power, are low cost and have low maintenance requirements. They also have a low acoustic signature due to lack of vibration, and are applicable to both single- and multi-phase flows.

In EHD pumping, an electrical body force is generated in the fluid by the interaction of electric fields with the charges in a dielectric fluid. Several different types of EHD pumps have been researched, including (a) ion drag EHD pumps (Darabi et al. 2002) (b) induction EHD pumps(Wawzyniak et al. 2000), and (c) conduction EHD pumps (Feng and Seyed-Yagoobi 2004).

EHD pumping mechanisms are classified according to the way that the charges are established in the fluid medium. In ion drag EHD pumping, charges are injected directly at the fluid/electrode interface by means of a corona source. The charge injection typically occurs at regions of high electric field gradients (Chang 1991) and hence the discharge occurs at the sharp edges of the electrodes where the electric field gradient is highest. These free charges move along the electric field due to the Coulomb force as shown schematically in Fig.2.1. The forces exerted on these free charges are transmitted to neutral molecules by viscosity which can result in bulk motion of the
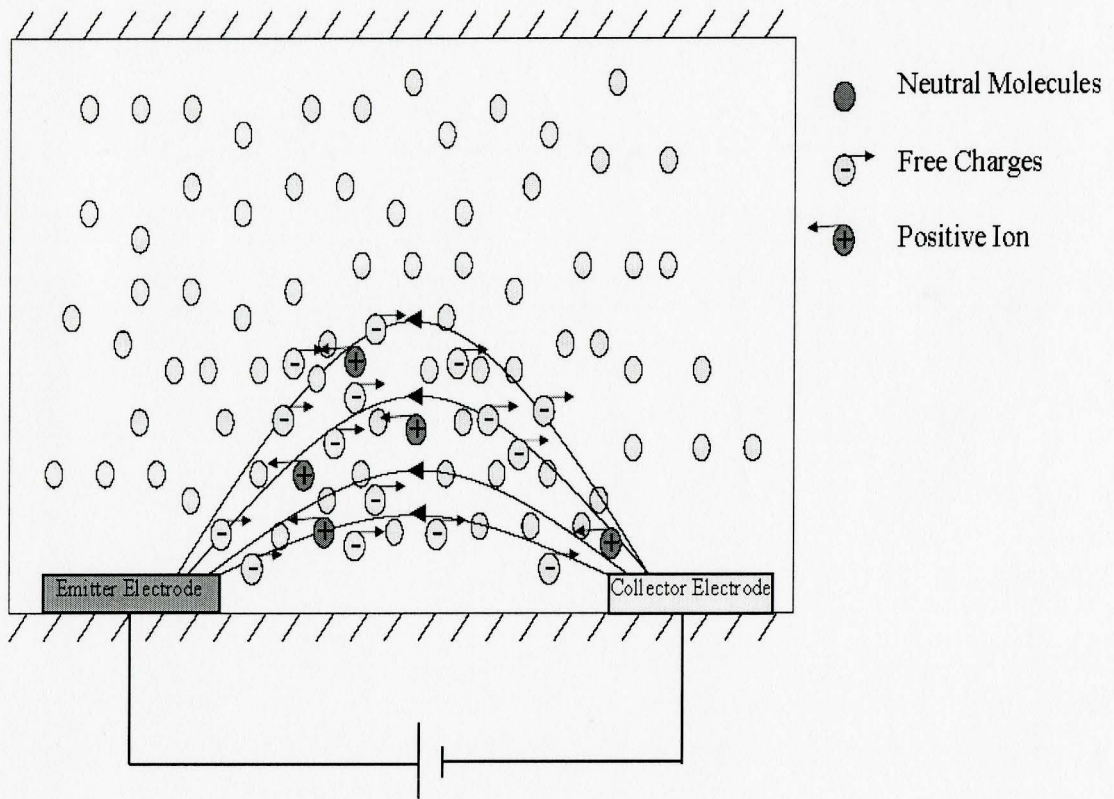
Figure 2.1: Schematic of ion drag phenomenon

fluid. The fluid motion can modify both the charge density distribution and the electric field.

In induction EHD pumping, charges are induced due to a discontinuity or gradient of electric conductivity. A non-uniform electric field, established by a traveling electric wave for example, will exert a directional force on these induced charges, which can set the fluid into motion. The concept of induction EHD pumping was first proposed by Melcher (1966). Since electric conductivity gradients are insignificant in single phase isothermal fluids, different techniques such as stratifying

liquids by using layers of non-mixing fluids and seeding fluids with particles have been investigated. This concept can also be used in two phase systems and when temperature gradient exist, which results in permittivity and conductivity gradients.

Conduction EHD pumps utilize dielectric liquids of low electrical conductivity ($\sigma_e < 10^{-7}$ S/m). In dielectric fluids under a electric field, conduction is due to positive and negative ions produced by the dissociation of neutral molecules

$$A^+B^- \underset{K_r}{\overset{K_d}{\leftrightarrow}} A^+ + B^- \tag{2.1}$$

where K_d and K_r are the dissociation and recombination rate constants, respectively. In the absence of an electric field, the dissociation and recombination rates are in equilibrium. When an electric field greater than a certain threshold (about 1kV/cm, depending on fluid characteristic) is applied, the dissociation rate increases while the
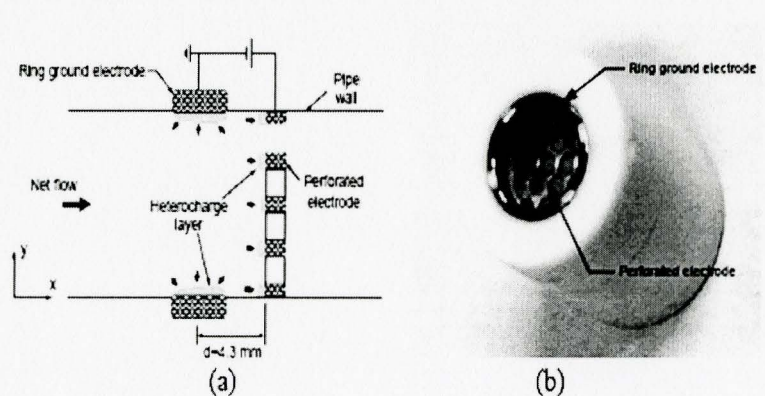
Fig.2.2.EHD conduction pump electrode configuration. (a) Schematic; (b)Picture (Feng and Seyed-Yagoobi 2004)

recombination rate is independent of the electric field and remains constant. Therefore, at a sufficiently high electric field the dissociation rate will exceed the recombination rate, and heterocharge layers will form around a liquid/electrode interface. The charges will have opposite polarity of the adjacent electrode. While the bulk of the fluid is electrically neutral, the electrode geometry can be designed so that a net force is exerted on the bulk of the fluid. The configuration of the electrode geometry and prevention of ion injection by covering the sharp edges of the electrodes are highly effective on the performance of conduction EHD pumps. A conduction EHD pump with ring and perforated-disk electrode configuration developed by Feng & Seyed-Yagoobi (2004) is shown in Fig.2.2.

2.3 EHD Phenomenon Governing Equations

In this section the governing equations of injection induced EHD flows are presented. The interrelation of the fluid dynamic and electrostatic equations makes it very difficult to obtain analytical solution in most cases. Nevertheless, an understanding of the governing equations is important for development of EHD pumps.

Electrical Equations

Maxwell equations

There are two distinct Galilean electromagnetism limits which are electroquasistatic where $E > c^{\cdot}B$, and magnetoquasistatic where $E < c^{\cdot}B$. E, c, and B are electric field, light speed, and magnetic field, respectively. These limits show the

relative significance of the magnetic field compared to the electric field. The general form of fourth Maxwell's equation (Chang et al. 1995) is

$$\nabla \times \mathbf{B} = \sigma.\mu.\mathbf{E} + \varepsilon.\mu.\frac{\partial \mathbf{E}}{\partial t} \qquad (2.3)$$

where σ, μ, and ε are electric conductivity, magnetic permeability, and electric permittivity, respectively.

From this equation, Atten and Castellanos (1995) obtained the relation between the electric field E, magnetic field B, light speed c, and electric conductivity σ as

$$E\,/c\dot{}B \sim 1/\sigma \qquad (2.4)$$

Therefore, in electrohydrodynamics where dielectric fluids with low electric conductivity are used as working fluids, $E > c\dot{}B$ and Maxwell's equations fall into the electroquasistatic limit. On the other hand, for liquids with high conductivity such as liquid metals, the magnetic force becomes dominant. Therefore, the phenomenon is in the magnetohydrodynamics (MHD) domain. In the electroquasistatic limit, the magnetic field can be eliminated and Maxwell's equations reduce to Poisson or Laplace equations (Chang et al. 1995)

$$\nabla \bullet \mathbf{E} = \frac{\rho_e}{\varepsilon} \qquad (2.5)$$

$$\nabla \times E = 0 \qquad (2.6)$$

The conservation of charge is

$$\frac{\partial \rho_e}{\partial t} + \nabla.\mathbf{J} = 0 \tag{2.7}$$

where the charge current density J is defined as the total charge flux due to bulk motion of fluid.

Constitutive law for current density

In accordance with the constitutive law for current density, two different regimes can be designated for dielectric fluids: 1.Ohmic regime and 2.Non-ohmic regime. The regime depends on the electric field intensity rather than the fluid property. In the ohmic regime, where Ohm's law is valid, the current density (Chang et al. 1995) is

$$\mathbf{J} = \sigma\mathbf{E} + \rho_e.\mathbf{u} \tag{2.8}$$

where **u** is the liquid velocity. Most liquids show ohmic behavior at a low electric field. At high electric fields, charge injection can occur at solid-liquid interfaces because of the presence of high electric field gradients. When charge injection becomes the main source of free charges in the liquid, Ohm's law fails to be valid. In a non-ohmic regime, if we assume that only one type of charge is injected into an absolutely insulating medium ($\sigma=0$), the current density (Chang et al. 1995) is

$$\mathbf{J} = \pm\rho_e.\mathbf{K}.\mathbf{E} - \mathbf{D}.\nabla.\rho_e + \rho_e.\mathbf{u} \tag{2.9}$$

where K, ρ_e, and D are ionic mobility, unipolar charge density, and molecular diffusion coefficient. The current density components on the right-hand side of the equation are migration current, diffusion current, and convective current, respectively. Migration charge current accounts for the motion of ions relative to the bulk of the fluid with velocity equal to K.E. The molecular diffusion is usually negligible under high electric field. The convection charge current is due to bulk fluid movement. If the migration velocity K.E is one order of magnitude larger than **u** and the divergence of the migration current flux is more than an order of magnitude larger than the divergence of the convective current flux, then $\rho_e.\mathbf{u}$ can be neglected from eq.2.9.

Fluid Dynamic Equations

The coupling of the ion transport equations with the fluid dynamics equations can be made by adding an electrical body force term to the momentum equation. For single phase incompressible flow, the conservation of mass and momentum are

$$\nabla.\mathbf{u} = 0 \qquad\qquad (2.10)$$

$$\rho[\frac{\partial u}{\partial t} + (\mathbf{u}.\nabla)\mathbf{u}] = -\nabla p + \rho.\mathbf{g} - \nabla.\tau + \mathbf{F}_e \qquad\qquad (2.11)$$

where p, τ, and F_e are pressure, mechanical stress tensor and electrical body force, respectively. The electric body force is the driving force in EHD pumps. Stratton (1941) used the conservation of energy equation to calculate the increment of energy in the presence of an external electric field E, and charge density ρ_e and obtained the following expression for the electric body force

$$\mathbf{F}_e = \rho_e . \mathbf{E} - \frac{1}{2} E^2 . \nabla \varepsilon + \frac{1}{2} \nabla [E^2 . \rho . \left(\frac{\partial \varepsilon}{\partial \rho} \right)_T] \qquad (2.12)$$

where ε and ρ are dielectric constant and density. The electric body force consists of three terms. The first term is the electrophoretic force or Coulomb force, and is the force exerted on a charge in an electric field. Since ρ_e is the net charge density, $\rho_e.E$ represents the net force acting on the fluid due to the Coulomb force.

The second term is the dielectrophoretic force, and is due to electric permittivity gradients in nonhomogenous dielectric liquids. The sign of the force is independent of the electric field contrary to the electrophoretic force. By expanding this term, it can be shown that this force is negligible in an incompressible single phase flow where there is no significant thermal gradient

$$\frac{1}{2} E^2 . \nabla \varepsilon = \frac{1}{2} E^2 \nabla [\left(\frac{\partial \varepsilon}{\partial \rho} \right)_T \nabla \rho + \left(\frac{\partial \varepsilon}{\partial T} \right)_\rho \nabla T] \qquad (2.13)$$

The third term is the electrostrictive force, which is a result of an inhomogeneous electric field or gradient in density. Since it is the gradient of a scalar, it is usually treated as a modification of liquid pressure

In single phase incompressible ion-drag pumping where there is no significant temperature gradient, the main driving force is the Coulomb force. Therefore, in order to improve the pump performance, the electric field and/or the charge density can be increased.

2.4 Literature review of liquid EHD pumps

Ion drag pumps

The physical mechanisms of ion drag EHD pumping have been studied since the late 1950's (Stuetzer 1959). Stuetzer based his work on the "corona wind" theory (Chattock 1901) and developed a model for plane, spherical, and cylindrical electrodes based on unipolar charge assumption. From experiments, he concluded that the pressure generation was proportional to the applied current and inversely proportional to the electric mobility. He observed different regions of the current-voltage characteristics and achieved a maximum pressure of 2 kPa with needle-cylinder electrodes and castor oil as working fluid.

Based on Stuetzer's work, Pickard (1963) derived a correlation between the electric field and pressure generation for a configuration with two flat parallel plane electrodes. Assuming that the Coulomb force is the main driving force in single-phase ion drag EHD pumps, he obtained a correlation for pressure by eliminating charge density from Poisson and Navier-Stokes equations as

$$P = \frac{9}{8}.\varepsilon.E_o^2 \qquad (2.14)$$

where E_o is the average electric field between the electrodes. The experimental results (Pickard 1963) for both static and dynamic cases were found to be in agreement with equation 2.14.

The electrode geometry has an important effect on the performance of ion drag EHD pumps. Several different electrode geometries have been investigated in order to improve pump performance and increase the efficiency (Asano et al. 1999; Rada 2004; Richter and Sandmaier 1990). Asano et al. (1999) presented an ion drag EHD pump with needle-cylinder electrodes. They observed that the radius of the needle heads had a significant effect on the breakdown voltage. They also found that the number of needles affected the pump performance, and that there were an optimal number of needles for a certain tube diameter. A maximum pressure head of 2800 Pa was achieved at an applied voltage of 29 kV with silicon oil as the working fluid. Rada (2004) designed a meso-scale ion-drag EHD pump for cooling applications with two electrode rings, and emitter needles around its edge. Applied voltages were significantly high because of higher inter-electrode gap distances. Maximum pressure heads of 2000 Pa at 30 kV and 160 Pa at 12 kV were achieved with HFE-7100 and R-134, respectively.

The first EHD pump at the microscale was fabricated by Richter and Sandmaier (1990) that consisted of two 3 mm × 3 mm silicon grid electrodes with a 350 µm electrode spacing. The silicon electrodes were manufactured with 30 µm orifices and a thickness of 35 µm. A maximum pressure of 2480 Pa was achieved at an applied voltage of 700 V with ethanol as the working fluid. The applied voltage was considerably smaller compared to macro-scale EHD pumps due to the small electrode spacing, which improved pump performance and efficiency.

Wong et al. (1997) used laser micromachining to fabricate ion drag EHD pumps with two different designs at Sandia National Laboratory. The first design had silicon

parts stacked on top of each other, while in the other design silicon parts were bonded back to back, which reduced the electrode spacing down to 102 μm. They used a Nd:YAG laser to bore an array of orifices on the silicon wafer. With the second design, a pressure head of 287 Pa was obtained at applied voltage of 120 V with propanol as the working fluid.

Ahn and Kim (1998) designed and fabricated an ion drag micropump with planar electrodes on a glass substrate. A simple one mask process was used to fabricate the electrodes, with an electrode spacing of 100μm and electrode double spacing of 200μm. A total of 30 pairs of electrodes were fabricated in a 30 mm long micro channel. They observed that the pressure and flow rate were proportional to the square of the applied voltage, and reported a maximum flow rate of 50 μm/min at an applied voltage of 110 V with ethanol as the working fluid.

More recently, Darabi et al. (2002) developed an ion drag micropump with tooth shaped emitter electrodes with solder bumps. The non-planar electrode design improved the pump performance compared to planar electrodes with the same electrode spacing. The micropump with tooth shaped planar electrodes generated 500 Pa at an applied voltage of 1000 V whereas the micropumps with bump electrodes generated the same pressure head at an applied voltage of 500 V with HFE-7100 as working fluid.

The effect of inter-electrode spacing and inter-pair spacing (gap between each pair of electrodes) was investigated by Benetis (2005) and Foroughi et al. (2005). Decreasing the inter-electrode spacing was observed to increase the pressure generation, but break down occurred at lower voltages. Foroughi et al. (2005)

investigated the effect of inter-electrode spacing and inter-pair electrode spacing in ion drag micropumps for cryogenic spot cooling with saw tooth shaped gold electrodes. One micropump had an inter-electrode spacing of 20 μm, and double inter-pair spacing of 80 μm, while the other had inter-electrode spacing and double inter-pair spacing of 50 μm and 200 μm, respectively. The micropump with smaller electrode spacing generated higher flow rates at lower voltage, with a maximum flow rate of 10 mL/min at 500 V.

Based on Foroughi's work, Darabi and Wang (2005) fabricated an ion drag EHD pump with saw-tooth/plane shaped electrodes with a 20 μm inter-electrode spacing. The electrode inter-pair spacing was reduced from 80 μm to 40 μm and the number of electrode stages increased from 135 to 200 stages. The pump was tested with both liquid nitrogen and HFE 7100, but pressure head and flow rate were only measured for HFE 7100. A flow rate of 3.9 g/min was achieved at a pressure head of 180 Pa. Kano and Takahashi (2006) developed an ion drag EHD micropump from a series of 0.3 mm stainless steel wires. The dimensions of the pump were 30 mm × 30 mm × 4.9 mm with 1 to 5 electrode stages. The electrode spacing was varied from 0.2-3.4 mm. The results showed the maximum pressure generation of the pump with inter-electrode spacing of 0.2 mm was ten times higher than the pump with inter-electrode spacing of 2 mm.

Bryan (1990) and Castaneda and Seyed Yagoobi (1991) investigated the effect of the number of electrode stages on ion drag EHD pump performance. Castaneda and Seyed Yagoobi (1991) performed tests with Dodecylbenzine, Conoco O. S. 260-P

industrial oil, kerosene, and Texaco 0600 oil and found that having several stages improved the performance of EHD pumps. They concluded that the pressure generation and current were linearly proportional to the number of electrode pairs. A maximum velocity of 15 cm/s was achieved at an applied voltage of 20 kV with dodecylbenzine as the working fluid. Castaneda and Seyed Yagoobi (1991) tested an axisymmetrical ion drag EHD pump with up to thirteen pairs of electrodes. Twenty-gauge tin copper wire circles were press fitted on the loop wall on each electrode. The inter-electrode spacing and inter-pair spacing were 8 mm and 15 mm, respectively. The results showed that by increasing the number of electrode pillars, the pump performance improved drastically. They also showed that the current is linearly proportional to the number of electrode pairs. A maximum pressure of 40 Pa was obtained at an applied voltage of 28 kV that resulted in 14 μA current.

Benetis et al. (2003) investigated the effect of the channel height on back flow pressure and flow rate in a planar ion drag micropump with HFE-7100 as the working fluid. They suggested that there is an optimum value for the channel height.

Fluid properties can have a significant effect on the performance of EHD pumps. Crowley et al. (1990) proposed the first model for ion-drag pumps to account for the working fluid properties. By modeling all three charge flux components (migration, convection, and conduction), they showed that a fluid with high conductivity and low viscosity resulted in a high velocity, while a low conductivity and mobility increased the efficiency. Since mobility and viscosity are inversely proportional, EHD pumps can not operate at both maximum efficiency and flow rate.

Bryan and Seyed-Yagoobi (1991) studied the effect of different working fluids on ion drag pumping by using dodecylbenzine at different doping levels. Subsequently, they experimentally investigated an ion-drag pump using electrodes designed from a fluid mechanics standpoint (Bryan and Seyed-Yagoobi 1992). In this case, the ions were injected into the fluid within the viscous boundary layer where the viscous shear stresses are highest. The rationale here was that the electrical body forces could be directed at the regions that would be most beneficial in improving the pump performance. The pump was tested with doped and undoped oil. They found that increasing the oil electrical conductivity levels reduced the pumping velocity.

Colleti and Bozzo (1996) investigated the effect of different working fluids on the correlation between applied voltage and pressure generation in ion-drag EHD pumps using a pump with two plane parallel electrodes in a 30 mm polymethylmethacrylate (PMMA) housing. The collector electrode was a 25 mm stainless steel disk of 170 μm mesh and the emitter electrode was a 27 mm drilled brass disk. Dodecylbenzine, castor and silicon oil were tested under static conditions with different electrode spacing that ranged from 0.5mm-3.5mm. They found a quadratic correlation between pressure head and applied voltage with castor and silicon oil, while the correlation had a more linear trend using dodecylbenzine. Maximum pressure of 450 Pa at 37 kV for castor oil, 50 Pa at 22 kV for dodecylbenzine, and 800 Pa at 37 kV for silicon oil was reported with 3.5 mm electrode spacing.

There are only a few studies in which the reliability and durability of EHD pumps have been addressed (Blologna et a. 1993; Malakhov 1999; Benetis 2005).

Bologna et al. (1993) conducted a life service test on an ion drag EHD pump. Three identical cells were tested with filtered and vacuum degassed kerosene, transformer oil, and polymethylsiloxane-5 (PMS-5). The pump performance with purified liquid declined gradually after 200 hours of operation. Non-filtrated PMS-5 behaved differently, and the pump performance was degraded from the start. Malakhov (1999) addressed the time service issue by testing a two-stage pump under static and dynamic conditions with kerosene as the working fluid. When the kerosene was not exposed to atmosphere, the pressure head and current were stable. When the system was exposed to the environment, the additional impurities from the atmosphere enhanced the sedimentation process on electrodes and degraded the pump performance. Benetis (2005) conducted a service test of about 300 hr on different micropumps and found that only the collector electrodes deteriorated. The pump performance deteriorated significantly in less than 10 hours with no significant degradation of electrodes. The performance degradation was attributed to degradation of the working fluid properties. However, after further use the electrode surfaces had noticeable defects. It was concluded that some of the electrons do not return to the current path; instead, these electrons cause dissociation of working fluid and participated in chemical reactions with impurity molecules like oxygen which results in working fluid electrical properties degradation as well as electrode deterioration.

There have been several attempts to numerically simulate EHD pumping. Darabi and Rhodes (2006) numerically simulated an ion drag EHD pumps using commercial CFD software, FIDAP. A 2-D cross section of electrodes was used as the

domain. The effect of applied voltage, channel height, inter-electrode spacing, inter-pair spacing, and the ratio between inter-electrode spacing and inter-pair spacing were investigated numerically. The numerical results showed that for a given channel height there is an optimum value for the electrode spacing/electrode double spacing ratio, which was in agreement with experimental results. Table 2.1 presents a summary of the experimental studies on ion drag EHD pumping.

Table 2.1 Overview of experimental studies of ion drag pumps.

Reference	Electrode Geometry	Electrode spacing	No. of electrode stages/ Electrode double spacing	Fluid			Applied Voltage	Max. Flow rate/ Pressure Head
				Mobilitiy m2/V.S	Viscosity mPa.S	Density kg/m3		
Stuetzer (1959)	Kerosene/ Silicon Oil	0.6-10mm	1 stage/NA	3E-07 35E-07	1.9 130	860 1040	Up to 30 kV	N.A.;1.6 kPa
Pickrd (1963)	Acetone	2.5-15mm	1 stage/NA	6.80E-08	0.29	780	Up to 10 kV	.17 cm/sec; 2 Kpa
Baryan (1990)	Dedocylbenzine	5 mm	10 stages	2.47E-10	8.09E-02	829	Up to 25 kV	15 cm/s; 112 Pa
Castaneda and Seyed-yagoobi (1991)	R 11	8 mm	13 Stage/ 15 mm	4.68E-08	4.27E-01	1453	Up to 25 kV	20 cm/s; 50 Pa
Richter and Sandmaier (1990)	Ethanol	350 μm	1 Stage/ N.A	1.70E-08	1.20	790	Up to 700 V	N.A.;2480 Pa
Richter and Planter (1991)	Ethanol	350 μm	1 Stage/ N.A	1.70E-08	1.20	790	Up to 700 V	14 ml/min; 2.5 kPa
Colleti and Bozzo (1996)	silicon oi	0.5-3.5 mm	1 Stage/ N.A	3.50E-06	130	1040	Up to 37 kV	N.A.; 800 PA
Wong, Chu, et al. (1997)	Propanol	102 μm	1 Stage/ N.A	2.25	8.90E-09	980	Up to 120 V	N.A.; 187 Pa
Ahn and Kim (1998)	Ethanol	100 μm	30 Stage/ 200 μm	1.70E-08	1.20	790	Up to 100 V	50 μl/min; 200 Pa

Continue of Table 2.1 Overveiw of experimental studies of ion drag pumps.

Reference	Electrode Geometry	Electrode spacing	No. of electrode stages/ Electrode double spacing	Fluid			Applied Voltage	Max. Flow rate/ Pressure Head
				Mobilitiy m2/V.S	Viscosity mPa.S	Density kg/m3		
Asano et al. (1999)	Silicon Oil	2-8mm	1 stage/NA	3.50E-06	130	1040	Up to 30 kV	N.A.;2.8 kPa
Darabi et al. (2002)	HFE-7100	50-100μm	50-95 Stages/50-100μm	1.31E-08	3.80E-01	1402	Up to 700 V	N.A.; 700 Pa
Benetis and Ohadi et al. (2003)	HFE-7100	20-50μm	Not Reported/80-100μm	1.31E-08	3.80E-01	1402	Up to 500 V	7.92 ml/min;N.A.
Yang et al. (2003)	Ethanol	80 μm	Not reported	1.70E-08	1.20	790	Up to 100 V	87 nl/mi/N.A.
Rada (2004)	HFE-7100 R-134	2.5 mm	3 stage/5 mm	1.31E-08 2.08E-08	0.38 0.166	1402 1207	Up to 30 kV	N.A.; 2 Kpa N.A.; 160 Pa
Benetis (2005)	HFE-7100	50-100μm	100 Stages/ 100-200 μm	1.31E-08	3.80E-01	1402	Up to 500 V	15 ml/min; 750 Pa
Foroughi and Ohadi et al. (2005)	Liquid Nitrogen	20-50μm	135 Stages/ 80-200 μm	Not Reported	1.70E-01	808 (@77K)	Up to 500 V	10 ml/mi; N.A.
Darabi and Wang (2005)	HFE-7100	20μm	200 Stages/ 40 μm	1.31E-08	3.80E-01	1402	Up to 200 V	3.9 g/mi; 180 Pa
Kano and Takahashi (2006)	Dibutyl-sebacate	0.2-3.4 mm	5 Stages/ 5 mm	2.10E-09	9.4	940	Up to 1 kV	N.A.; 350 Pa

Induction pumps

Induction pumping is limited to two phase and/or non-isothermal systems because of its dependency on conductivity or permittivity gradients of the working fluid. Therefore, induction pumping is not effective for cooling applications using a single phase isothermal fluid.

The principle of traveling wave-induced charges in a liquid with a permittivity and/or conductivity gradient at the liquid surface was established by Melcher and Firebaug (1967). In order to have a conductivity gradient, a temperature gradient was imposed on corn oil with low electric conductivity. It was shown that charges are induced in the fluid by applying a traveling wave electric field perpendicular to temperature and conductivity gradients. Bart et al. (1990) fabricated an induction micropump in which a 1-kHz traveling wave of 200 V was used to move silicon oil with a maximum velocity of 9mm/s in a channel with a 20 μm depth.

More recently, Wawzyniak and Seyed-Yagoobi (2000) investigated induction pumping with a stratified liquid/vapor medium. The pump was tested with refrigerant HCFC-12, and it was observed that pumping was due to both interfacial and bulk effects. Brand and Seyed-Yagoobi (2003) investigated EHD induction pumping of a micro-liquid film for improving the heat transfer in heat exchangers through flow management. Maximum heat flux of 45 W/cm^2 was dissipated using refrigerant R-123 as working fluid.

Singhal and Garimella (2005) studied induction EHD micropumps that were integrated into microchannels for cooling systems. With a nozzle-diffuser structure, a

flow rate of approximately 50 mL/min was obtained for a pump with a diaphragm of diameter 2 mm and electrode width and spacing of 10 μm each. Singhal and Garimella (2006) developed an induction EHD micropump with a 500 nm thick layer of aluminum deposited to pattern electrodes with 18 μm electrode spacing. The micropump was tested with a mixture of potassium chloride (KCl) and deionized water. A maximum velocity of 18 μm/s was measure perpendicular to the electrodes using PIV.

Conduction pumps

Macro-scale EHD pumps require significant voltages in order to obtain a sufficiently high electric field. On the other hand, reducing the inter electrode gap distance leads to a high electrical field with low dc voltages in micro scale EHD pumps.

Despite the fact that the concept of conduction phenomenon has been known for a long time, conduction pumping was first studied analytically by Atten and Seyed-Yagoobi et al. (1999). They tested a pump with simple point/plane electrode with refrigerant R123 and n-hexane as working fluids. The pump performance was depended on the electric permittivity of the working fluid. The pressure head generated with n-hexane was about 4 times lower than R-123 where the permittivity of the n-hexane is about 5 times lower than R-123.

Subsequently, Atten et al. (2003) carried out extensive theoretical and numerical work and determined the feasibility of EHD pumping based on the conduction phenomenon. In their work a new arrangement of electrodes was

proposed. The electrodes consisted of a needle as the high voltage electrode and a ring as the ground electrode. They showed that the electrode configuration was an important factor in conduction pumping.

Feng and Seyed-Yagoobi (2004) utilized conduction pumping in a heat exchanger. They manufactured an EHD conduction pump that consisted of three pairs of stainless steel electrodes with gold coating. Each pair of electrodes had a 1.59mm perforated disc electrode and a ring ground electrode. A pressure head of 900 Pa was obtained at an applied voltage of 15 kV with R-123. In the same year, Jeong and Seyed-Yagoobi (2004) developed a conduction EHD pump with two different perforated disks and two different porous disks as the high voltage electrode and a ring electrode as the ground electrode. A pressure head as high as 1400 Pa was generated at an applied voltage of 18.5 kV with a 0.2 μm porous disk with refrigerant R-123.

Feng and Seyed-Yagoobi (2007) developed an analytical model for the performance of a conduction EHD pump. Based on their analytical model, they derived an expression for the pressure head as a function of applied nominal electrical field, flow velocity, and permittivity of working fluid. They concluded that heterocharge layer thickness increases if the flow is directed away from the electrode and decreases if directed toward the electrode surface.

Recently, Yazdani and Seyed Yagoobi (2007) numerically simulated a conduction pump. A parametric study on the heterocharge layer, flow structures and flow velocity effects on charge distribution were performed. The net flow rate was

drastically increased and then gradually decreased as the distance between the two electrode pairs was decreased. The enhancement and subsequent reduction of the net flow rate was clearly due to the elimination of negative interactions between the two electrode pairs and the increase in the viscous shear stress along the channel surface, respectively.

2.5 Summary

This chapter provides an overview of liquid EHD pumping phenomenon. Ion drag, conduction, and induction pumping mechanisms are discussed, along with their applications, advantages, and limitations.

The electrical and fluid dynamics governing equations were presented for ion drag pumping. Two Galilean electromagnetism limits distinguished between electroquasistatic and magnetoquasistatic. Electrohydrodynamics, where dielectric fluids are used, can be categorized under the electroquasistatic realm. The Maxwell equations were presented for this condition.

In ion drag phenomenon, charge injection occurs at solid-liquid interface; therefore, the constitutive law for current density in the non-ohmic regime was derived under unipolar charge injection assumption. Fluid dynamics and electric body force equations were also presented. It was shown that the Coulomb force is the main driving force for single phase incompressible flows in isothermal systems.

Finally, a literature review was presented in order to give a better understanding of existing work in this field. The progress and problems associated with electrohydrodynamics are presented.

Chapter 3: Micro-Fabrication Process of EHD Micropumps

3.1 Introduction

The advent of microfabrication techniques brought electro-mechanical systems into a new era. The ability to precisely define microscale structures along with low batch fabrication costs initiated a significant amount of research targeting microelectro-mechanical systems (MEMS). The objective of this study is to develop ion-drag EHD micropumps for cooling applications and investigate the effect of different geometrical design specifications on its performance. Ion-drag pumps have been studied extensively in the past and various manufacturing techniques and geometrical design specifications were investigated at the macro and microscale. However, none of these studies investigated micropumps with a 3-D electrode design. In this study, new electrode structures are devised and the corresponding microfabrication techniques are developed accordingly. This chapter presents the rational behind the design and manufacturing process of the ion-drag EHD micropumps.

3.2 Electrode Design

In most previous studies, ion-drag pumps were manufactured using precision machining. Generally, sharp angled geometries (e.g. needles, thin wires) are utilized as emitter electrodes with smooth shaped collector electrodes (e.g. thick wires, metal rings, flat plates). With advances in microfabrication techniques, two types of ion-drag EHD micropumps have been developed: (1) planar micropumps (Ahn and Kim 1998) in which the electrodes are placed on the bottom of the microchannel and (2) grid type electrode pumps (Richter and Plettner et al. 1991).

In grid-type micropumps, grid electrodes (e.g. perforated silicon wafers) are utilized in a channel perpendicular to the flow direction. This type of electrode design is typically suitable for channel diameter in range of a few centimeters. The pressure drop in these pumps depends on the grid shape, density, and surface roughness and the electrode geometry is limited by the silicon wafer thickness and etching techniques. In planar micropumps, on the other hand, the electrode geometry is limited by the mask feature size which is several μm and manufacturing process is very simple because of the 2-D structure of the electrodes. The effect of the planar electrodes on the pressure drop is minimal, which is mainly a function of microchannel height which can be reduced to tens of μm.

For single phase pumping applications, the main electric body force is the Coulomb force as outlined earlier. The Coulomb force can be increased by increasing the charge density within the fluid and/or by increasing the electric field. The charge injection occurs by corona discharge, primarily at the electrode edges because of the

higher electric field gradients in this region. In planar electrodes, due to the absence of sharp edges, there is a reduced corona discharge. In addition, in this design, the electric field density is high only near the electrodes (bottom of the microchannel), and decreases dramatically with increasing distance from the electrodes. Hence, the electric body force can be insignificant in the regions a short distance away from the electrodes.

The shortcomings of using planar electrodes can be overcome by using three-dimensional electrodes, albeit at the expense of more complexity in the microfabrication of the device. The use of 3-D electrode designs can increase the charge injection by introducing more edges and also establish a more homogenous electric field with a higher density over the entire flow domain.

For the present study, four different electrodes geometries: (1) planar symmetric electrodes, (2) planar asymmetric electrodes, (3) 3-D symmetric electrodes, and (4) 3-D asymmetric electrodes were investigated. The critical factors in the micropump design are the inter-electrode spacing d_{es}, inter-electrode pair spacing d_{eds}, distance between pillars d_p, pillar width W_p, channel height H, and number of electrode pairs N_e. Fourteen different micropumps were fabricated for this study, the dimensions of which are given in Table 3.1. To be consistent, the number of electrode pairs for all pump designs was kept constant at 100. The channel length is calculated accordingly to cover the gold electrode base. The height of the microchannel and micropillars are 100µm and 20µm, respectively.

The planar electrodes were designed in symmetric and asymmetric configurations as shown in Fig. 3.1. In the planar symmetric electrode (PE) configuration, the width of both the emitter and collector electrodes is equal to 40 μm whereas in the asymmetric planar electrode (APE) configuration the width of the collector electrodes are half the width of the emitter.

Micropillars were used to form two different 3-D electrode configurations. The 3-D symmetric electrode (3DE) design consisted of micropillar emitter and collector electrodes (as shown schematically in Fig. 3.2 and Fig. 3.3) whereas the 3D asymmetric electrode (3DAE) design consisted of micropillar emitter electrodes and flat collector electrodes (Fig 3.4).

Table 3.1 Micropumps design specifications.

| Micropump #	Electrode Geometry	d_{es} (µm)	d_{eds} (µm)	d_p (µm)	Ne	H(µm)	W (mm)
APE-S40	Asymmetric planar electrodes	40	80	N/A	100	100	5
APE-S80	Asymmetric planar electrodes	80	160	N/A	100	100	5
APE-S120	Asymmetric planar electrodes	120	240	N/A	100	100	5
3D-P80-S40	3-D Electrodes (pillars/pillars)	40	80	80	100	100	5
3DE-P80-S80	3-D Electrodes (pillars/pillars)	80	160	80	100	100	5
3DE-P80-S120	3-D Electrodes (pillars/pillars)	120	240	80	100	100	5
3DE-P120-S80	3-D Electrodes (pillars/pillars)	80	160	120	100	100	5
3DE-P160-S80	3-D Electrodes (pillars/pillars)	80	160	160	100	100	5
3DAE-P80-S80	3-D asymmetric electrodes (pillars/flat)	80	160	80	100	100	5
3DAE-P120-S80	3-D asymmetric electrodes (pillars/flat)	80	160	120	100 .	100	5
3DAE-P160-S80	3-D asymmetric electrodes (pillars/flat)	80	160	160	100	100	5
PE-S40	Planar electrodes	40	80	N/A	100	100	5
PE-S80	Planar electrodes	80	160	N/A	100	100	5
PE-S120	Planar electrodes	120	240	N/A	100	100	5
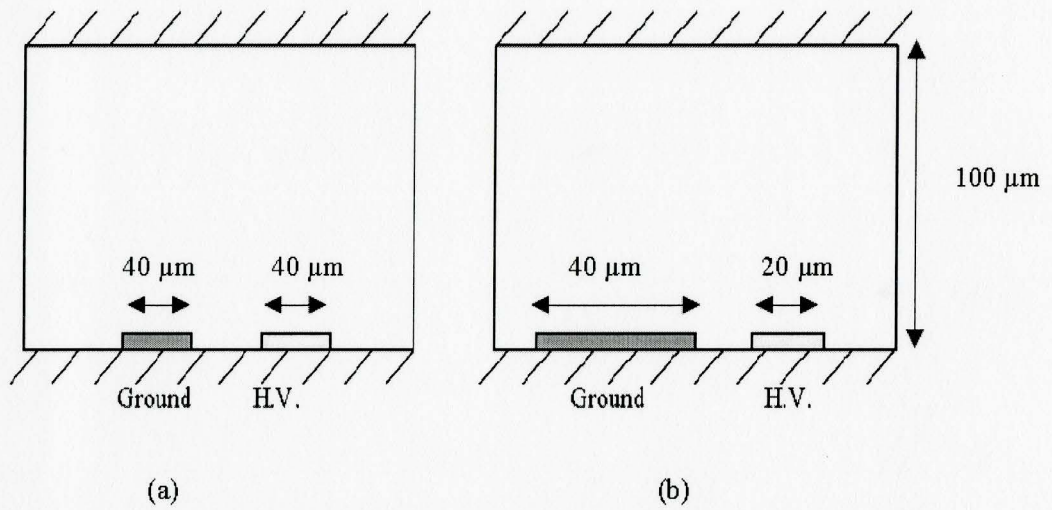
Fig. 3.1 Typical planar electrode geometry: (a) planar symmetric electrodes, (b) planar asymmetric electrodes.
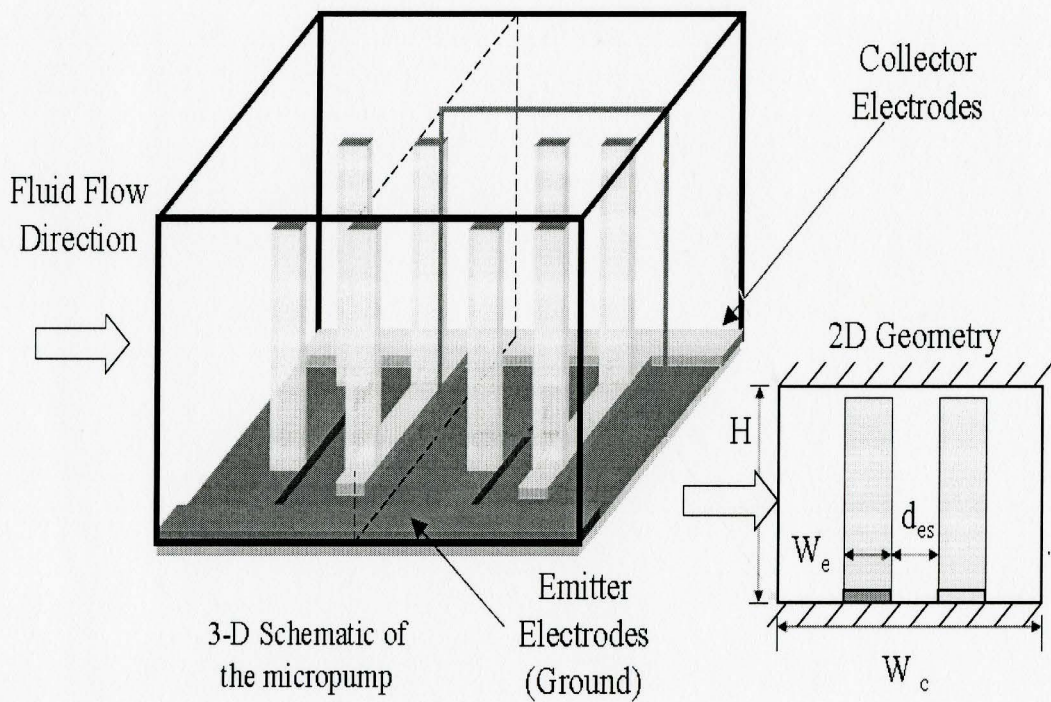
Fig. 3.2 Schematic EHD micropump with 3-D electrode structures (micropillars/micropillars).

Micropillar
Electrodes

Glass Substrate

Collector
Electrodes

Emitter
Electrode

Fig. 3.3. 3-D symmetric electrode design (micropillar emitter electrodes/ micropillars collector electrodes).

Micropillar
Electrode

Glass Substrate

Collector
Electrodes

Emitter
Electrodes

Fig. 3.4. 3-D symmetric electrode design (micropillar emitter electrodes/ planar collector electrodes).

3.3 Material and Working Fluid Selection

The materials for the pump substrate, electrodes, and microchannel were selected based on the EHD phenomenon and present microfabrication technology. For the 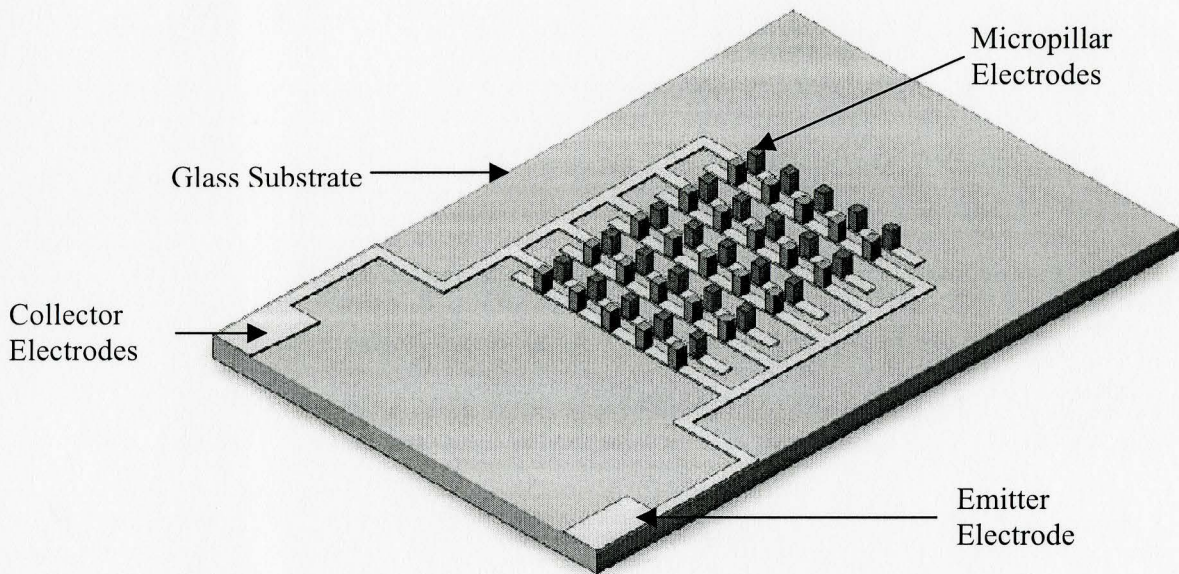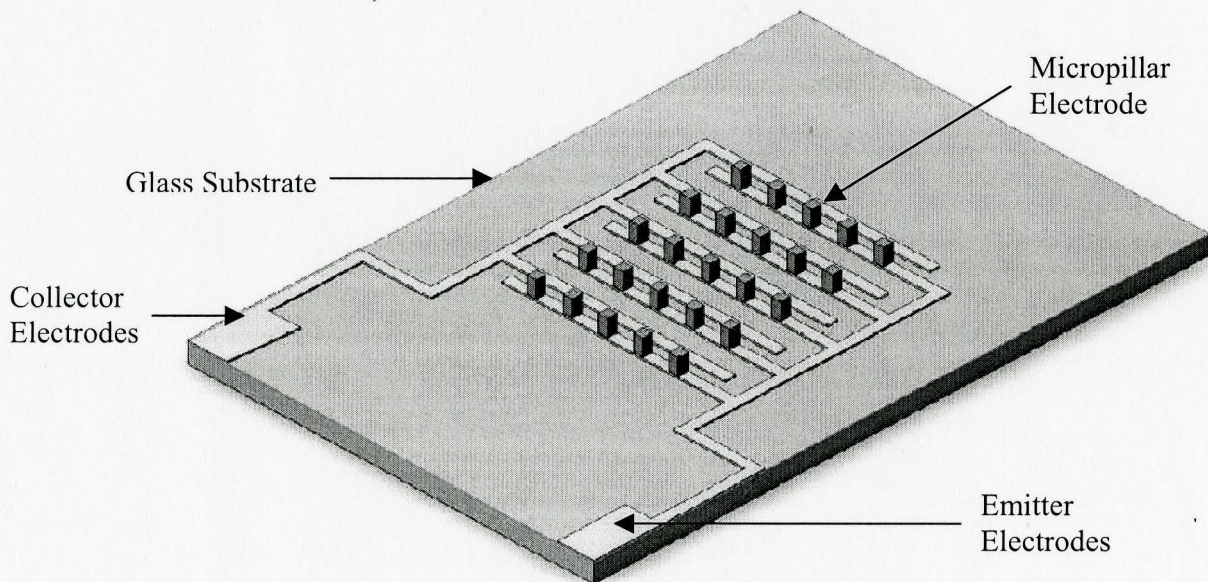pump substrate, glass was chosen because of its electric insulating properties to isolate the metal electrodes. The substrate also provides a flat smooth surface for the microfabrication of the electrodes.

The electron-beam evaporation technology was used for metal deposition because it gives a high control over growth rate and film thickness. However, this technique can not be used for thick film deposition, so an electroplating technique was used to fabricate the micropillars. From the microfabrication stand point, the electrode material should be selected so that there is good adhesion between the glass substrate, electrode base, and micropillars. Also, a good resistance to oxidation is an important factor for the electrode base material selection since it affects the electroplating process.

An important criterion for the electrode material selection is the ability of the metal to inject charges, which is a function of the metal work function. Fowler and Nordheim (1928) derived the following equation for the current density

$$J(E) = 1.545 \times 10^{-6} \frac{\beta^2 E^2}{\varphi} \exp(-6.83 \times 10^{-7} \frac{\varphi^{3/2}}{\beta E}) \qquad (3.1)$$

where E is the electric field strength, and β is a field enhancement factor which is related to the electrode geometry, and φ (eV) is the work function of the metal. The

Table 3.2 Work function of metals available at electron-beam deposition system

Metal	Au	Cr	Ni	Al	Pt
Work function (eV)	5.1	4.5	5.15	4.28	5.65

work function of the metals available at the McMaster University electron-beam vapor deposition system is listed in Table 3.2. Since the current density decreases with an increase of the work function, aluminum has higher charge injection properties compared to the other listed materials. Nevertheless, its low resistance to electrochemical corrosions makes aluminum an inappropriate candidate for the electrode material.

Chromium has a low work function, but it also has a low oxidation resistance. Therefore, despite its higher charge injection potential and adhesion to glass, chromium can not be used solely as an electrode base. Gold was selected for the electrode base because of its high resistance to electrochemical corrosion and oxidation which is crucial for electroplating. Since gold does not adhere to the glass substrate, a chromium layer is deposited as a seed layer for the gold deposition. Nickel was selected for the micropillars because of its resistance to electrochemical corrosion. Moreover, it is easy to electroplate a high aspect ratio structure using nickel.

The microchannels were fabricated by casting Polydimethylsiloxane (PDMS). PDMS is silicon-based organic polymer and it is widely used for rapid prototyping in

microfluidic devices. It is optically clear, non-toxic, nonflammable, and inert. The chemical formula for PDMS is $(H_3C)[SiO(CH_3)_2]_nSi(CH_3)$, where n is the number of the repeating monomers. After polymerization and cross linking, cured PDMS surface has hydrophobic properties.

The working fluid has a significant impact on the performances of EHD pumps. A high dielectric constant results in a high pressure generation, whereas a lower electric conductivity results in higher efficiency (Crowley et al. 1991). In this study, the micropumps are tested using Methoxynonafluorobutane (HFE-7100) as

Table 3.3 Physical Properties of different fluids under standard ambient temperature and pressure condition.

Property	Water	Ethanol	R-123	HFE-7100
Density (kg/m3)	1000	798	1464	1480
Dynamic Viscosity (mPa.s)	1	1.2	0.409	0.651
Thermal Conductivity (W/m.K)	0.595	0.14	0.077	0.069
Dielectric Constant	80	25.8	4.5	7.39
Ion Mobility (cm2/V.sec)	2.08E-08	1.70E-06	1.46E-08	1.31E-08
Molecular Weight (g/mol)	18	46	152.9	250
Boling Point (°C)	100	78.3	27.8	61
Specific Heat (kJ/kg.K)	4.184	2.845	1.035	1.18
Heat of Vapourisation (kJ/kg)	2260	855	229	111.6

working fluid. Methoxynonafluorobutane is a clear, colorless, nonflammable, and low-odor dielectric liquid with chemical formula of $C_4F_9OCH_3$ and commercial name of HFE-7100. This fluid has a lower global warming potential than hydrofluorocarbons (HFCs) which makes it more environmental friendly. HFE-7100 is a liquid under standard atmospheric conditions with a boiling temperature of 61°C. The molecular structure of HFE-7100 is shown in figure 3.5. Table 3.3 presents a comparison between physical properties of water, ethanol, refrigerant R-123, and HFE-7100 under standard ambient temperature and pressure condition..
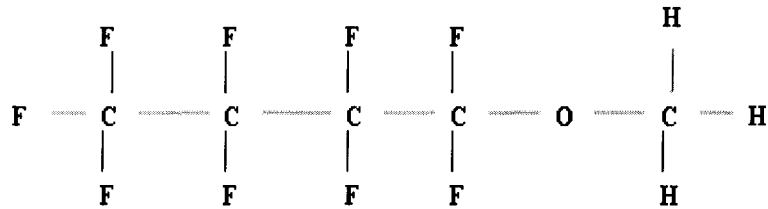
Fig. 3.5 Molecular structure of HFE-7100.

3.4 Microfabrication Process

The microfabrication process of the EHD pump can be divided into three major steps: (1) electrode fabrication, (2) microchannel fabrication and (3) integration of the electrodes with the microchannel. For the electrode fabrication, a two mask process is used to fabricate the high aspect ratio electrodes using microscale electroplating techniques as shown schematically in Fig.3.7. The first mask was used to pattern the mould for the micropillars while the second mask was used to pattern the electrode base. A typical mask drawing for the micropillars mould, electrode base, and microchannels is shown in Fig.3.6.

Fig.3.6 Designed mask drawing.

Au
Cr

(a) 1.Metal deposition of Cr and Au

AZ P4620

(b) Patterning AZ P4620 as pillars mould

Nickel
Pillars

(c) Nickel Electroplating

(d) Patterning electrode base

(e) Etching Au and Cr
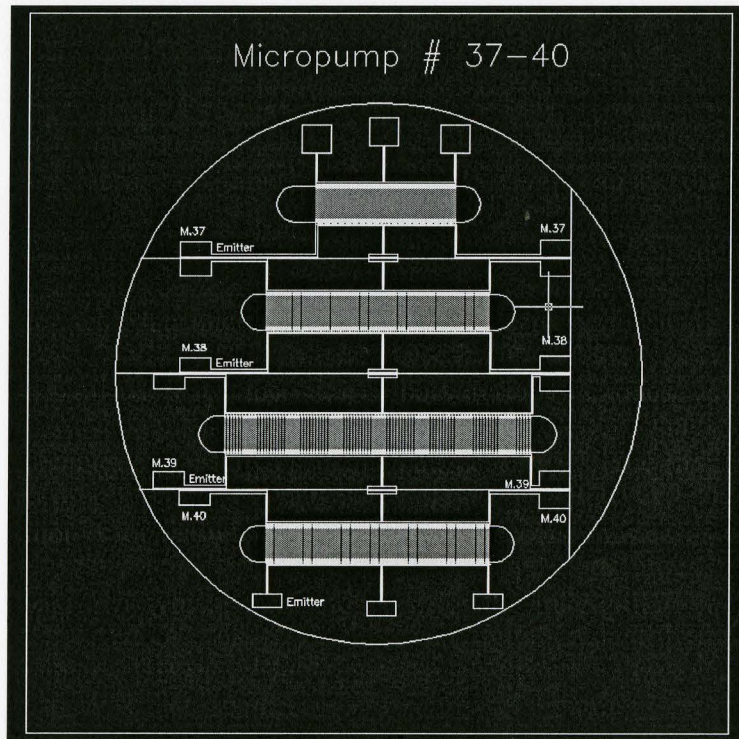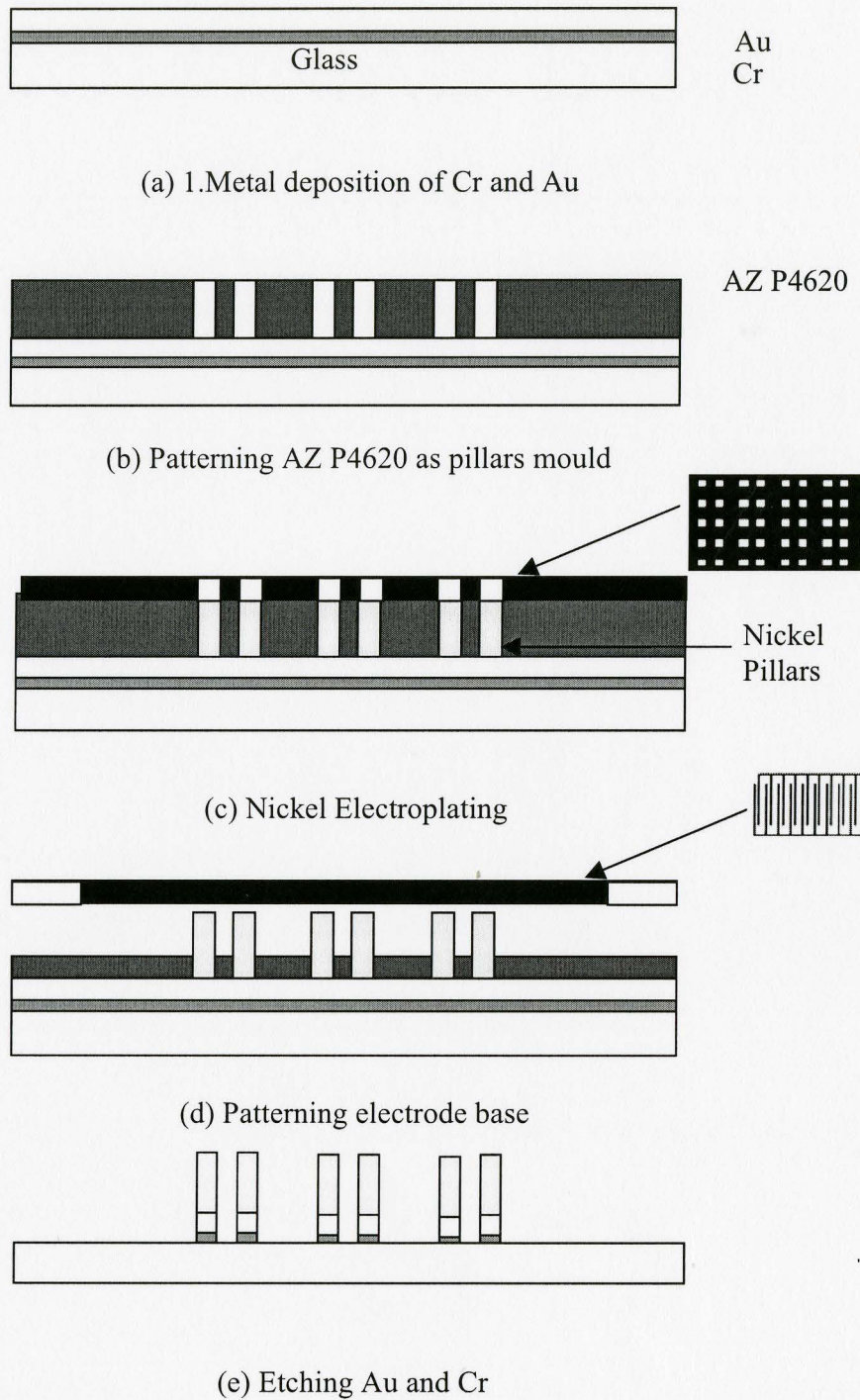
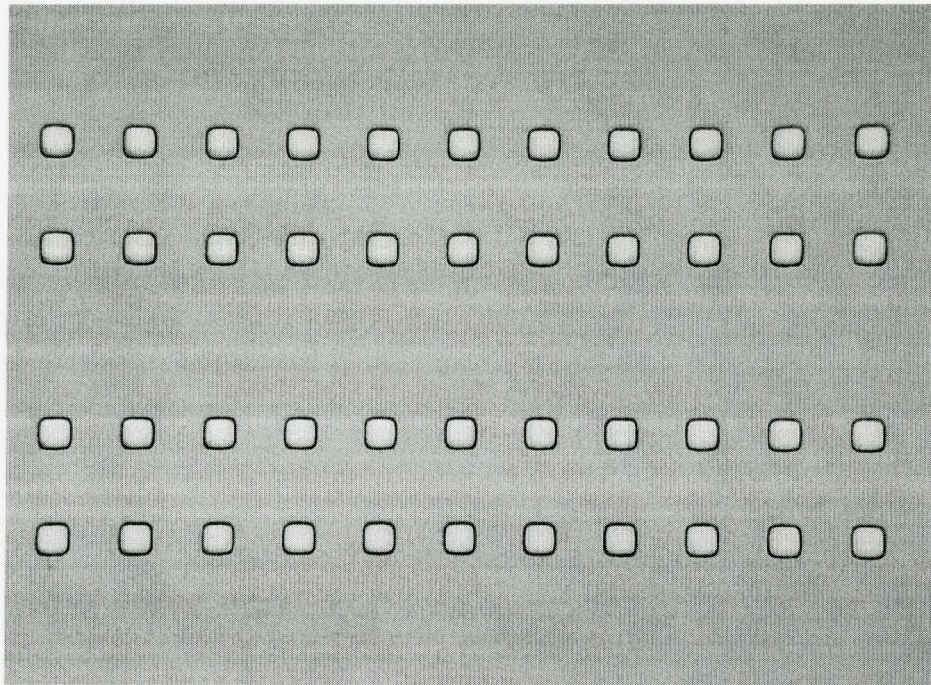Fig.3.7 Electrodes micro-fabrication process diagram.

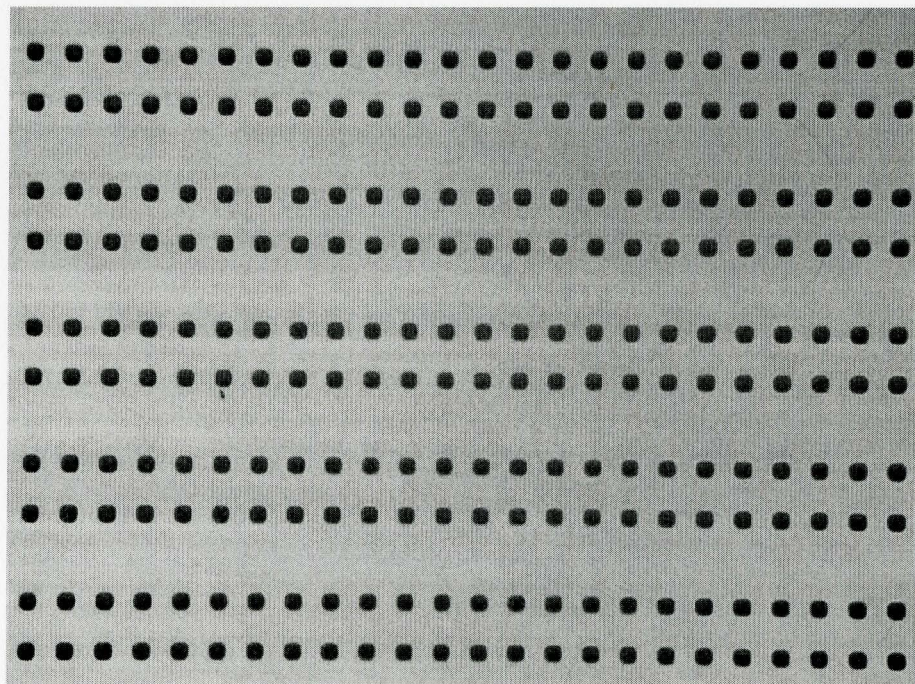Fig.3.8 Mould for the micropillar electrodes.

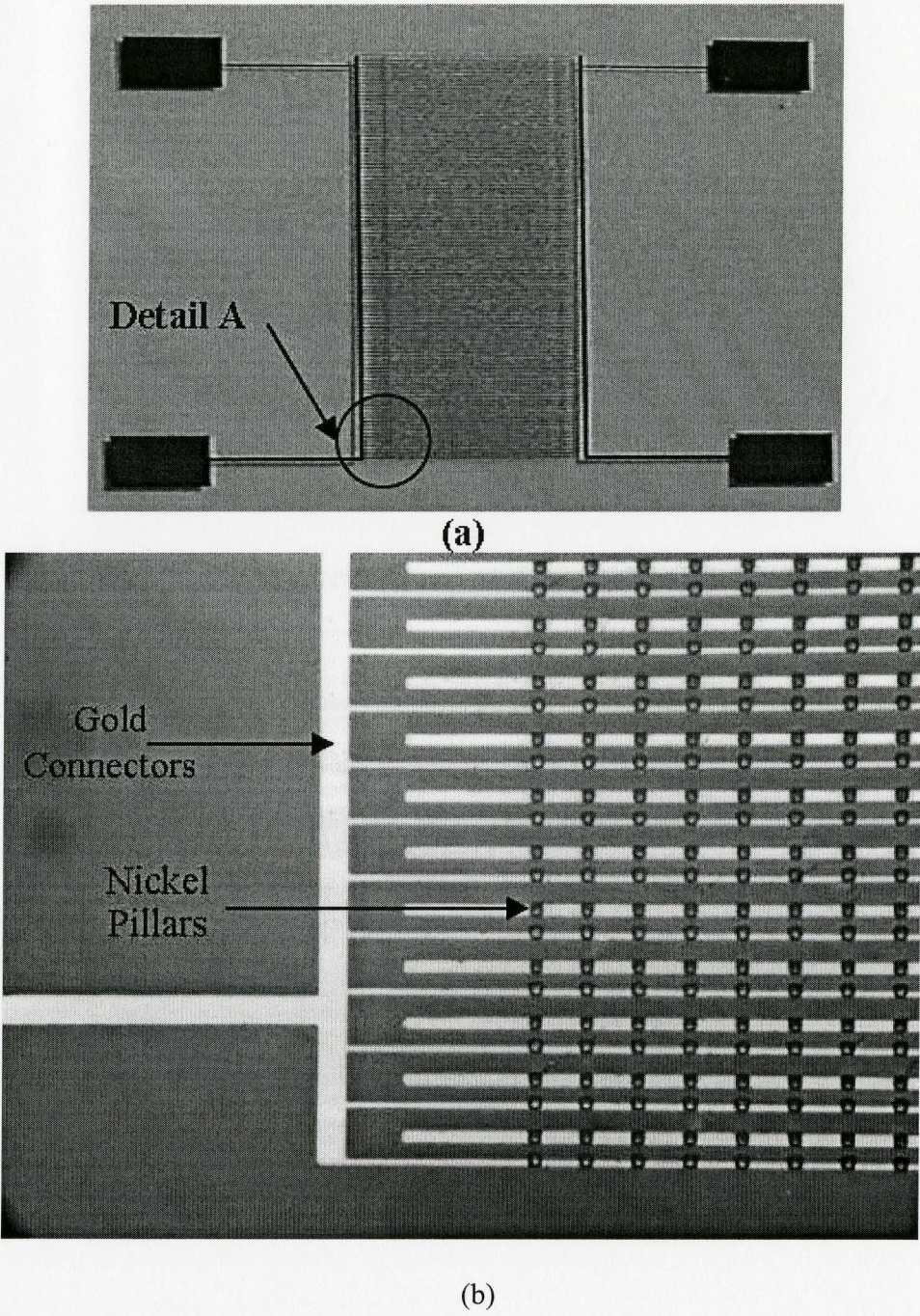Fig.3.9 Electroplated nickel micropillars.

(a)

(b)

Fig 3.10 Top view of gold electrode base with nickel pillars.

At the first step of the fabrication process shown in Fig. 3.7. (a), a layer of 100Å chromium and a layer of 2400Å gold were deposited on the glass substrate as a plating base. Chromium serves as an adhesion layer in order to bind the gold thin film to the substrate. The gold serves as the seed layer for subsequent electroplating. Subsequently, the wafer was plasma oxidized at 80 W for 1 minute to remove any organic residues and improve surface adhesion. A thick positive photoresist (AZ P4620 from MicroChem Corp.) was used to form the micropillar mold for electroplating. AZ P4620 was spun cast at 500 rpm for 30 seconds and ramped to 2000 rpm in 2 seconds. The sample was baked at 90 °C ramped to 120 °C for 6 minutes. After exposing for 65 seconds at 7.2 mJ/sec, the sample was developed in
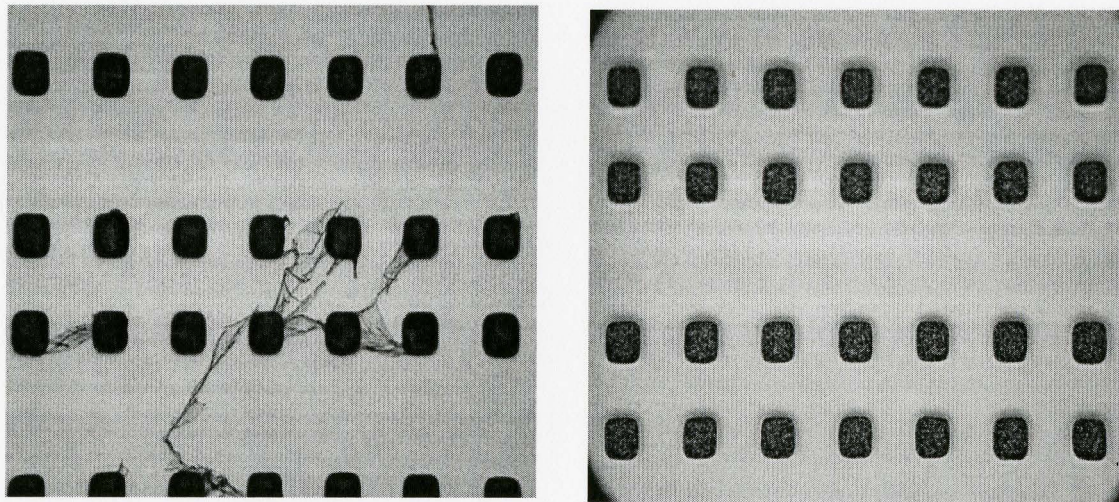
(a)   (b)

Fig. 3.11 Oxygen plasma etching of photoresist residues: (a) sample rinsed with acetone before plasma oxidization (b)sample after plasma oxidization

1:3 AZ K400 to DI water for 8 minutes. A picture of micropillar electrodes mould is shown in Fig.3.8.

Nickel was electroplated to fill the mold (Fig. 3.9). The nickel-plating solution consisted of 200 g/l nickel sulfate, 5 g/l nickel chloride, 30 g/l boric acid, and 30ml/l of wetting agent. With a current density of 10 mA/cm^2, the 20μm pillar structures were electroplated at a rate of 12μm/min. The photoresist was subsequently removed by rinsing the sample with acetone. It is important to remove any photoresist residues completely, since they can result in defects to the base electrode pattern and a short circuit. Therefore, the sample was plasma oxidized at 80 W for 5 minutes in order to completely remove the photoresist. Fig. 3.11 shows a sample before and after plasma oxidization. The photoresist residues were completely removed after plasma oxidization. Subsequently, S-1808 photoresist was spun cast at 3000rpm for 30 seconds. The sample was pre-baked at 110 °C for 90 seconds. The sample was exposed for 6 seconds at 7.2 mJ/sec to pattern the Cr/Au using the electrode base mask. Commercial gold etchant [Sigma-Aldrich] and a nickel compatible chromium etchant [Cyantek Corp. CR100] were used to etch the base electrode layer (Fig.3.10).

The microfluidic channels were fabricated by casting polydimethylsiloxane (PDMS) on top of an SU-8 (MicroChem Corp.) mould which was patterned to delineate the microchannel structure. A silicon wafer was plasma oxidized for 1 min at 50W in advance to improve adhesion properties. Su-8 100 was spun at 3000rpm on a silicon wafer for 30 sec to spread a 100μm thick layer. The resist was soft baked for 10min at 65°C, and for 30min at 95°C. the sample was exposed for 90 seconds at 7.2

mJ/sec using the microchannel negative mask. Following exposure, the sample was post baked for 1 min at 65°C, and for 10 min at 95°C. A 1:10 curing agent to PDMS mixture was used to cast the microchannels with a 100μm height. The cured PDMS channels were peeled off from the Su-100 mould, and holes were punched on them in order to attach glass tubing for the inlet and outlet of the pump (Fig.3.12).

The channels were adhered to the electrode glass sample using a combination of plasma oxidization and liquid PDMS as glue (Fig.3.12). The peeled PDMS microchannel was aligned on the electrode substrate relative to electrodes. Both PDMS channel and glass wafer were plasma oxidized for 1 minute at 50 W. Then a 1:3 curing agent to liquid PDMS mixture was poured on the microchannel border and
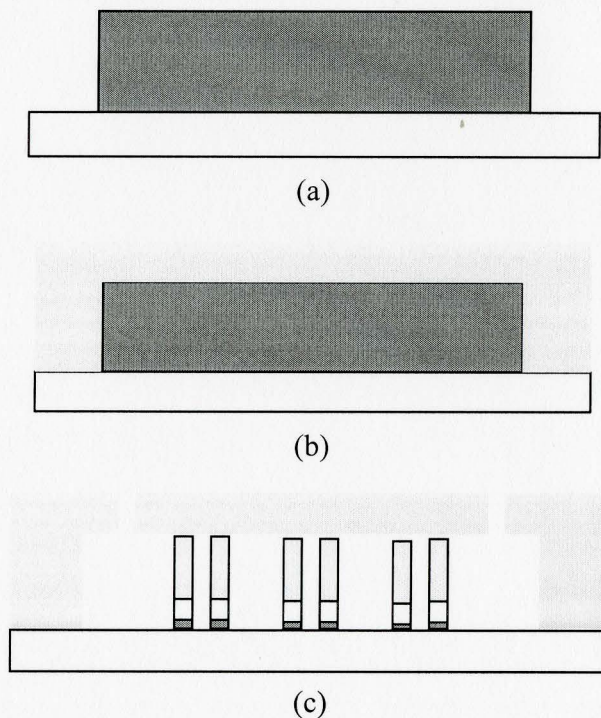
(a)

(b)

(c)

Fig. 3.12 PDMS microchannel fabrication and integration on the electrode substrate.

baked at 150°C. The PDMS prepolymer on the microchannel boundary bond the microchannel with the underlying glass layer. This prevents the leakage problems associated with PDMS microchannels with integrated electrodes.

3.5 Nickel Electroplating

Electroplating is a conventional and inexpensive way of depositing thin and thick films on conductive substrates without damaging the substrates. A typical electroplating cell consists of an anode (Nickel target), cathode (conductive substrate to be plated), aqueous metal solution (Nickel electroplating solution e.g., Nickel sulfate solution which contains Ni^{2+} and SO_4^{2-} ions), and a power supply. When the voltage is applied, the Ni^{2+} ions are attracted to the negatively biased cathode and the SO_4^{2-} ions are attracted to the positively biased anode. The Ni^{2+} ions gain electrons at the cathode and are deposited onto the surface of the sample. The anode or the Nickel target is etched to produce ions for the electroplating solution and electrons for the power supply.

Table 3.4 Nickel electroplating solution (Ahn et. al, 2005).

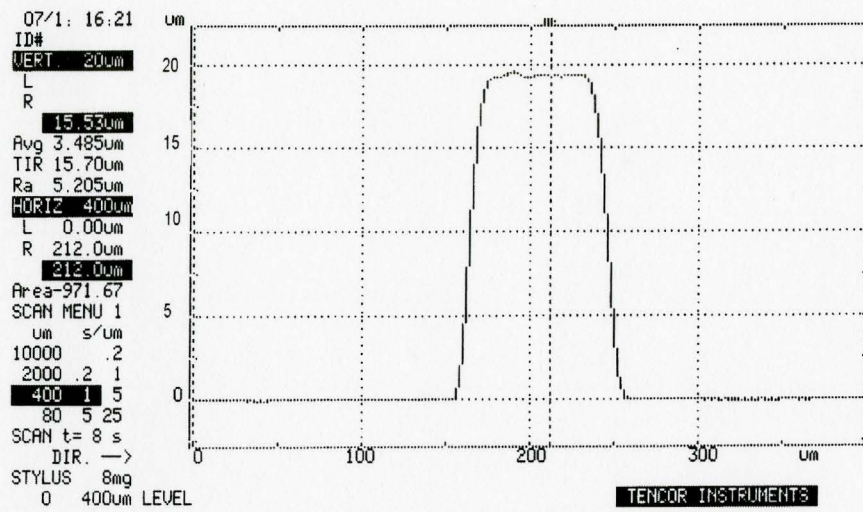| Material	Nickel Sulfate	Nickel Chloride	Boric Acid	Wetting agent
Quantity	200g/L	5 g/L	25 g/L	20 mL/L

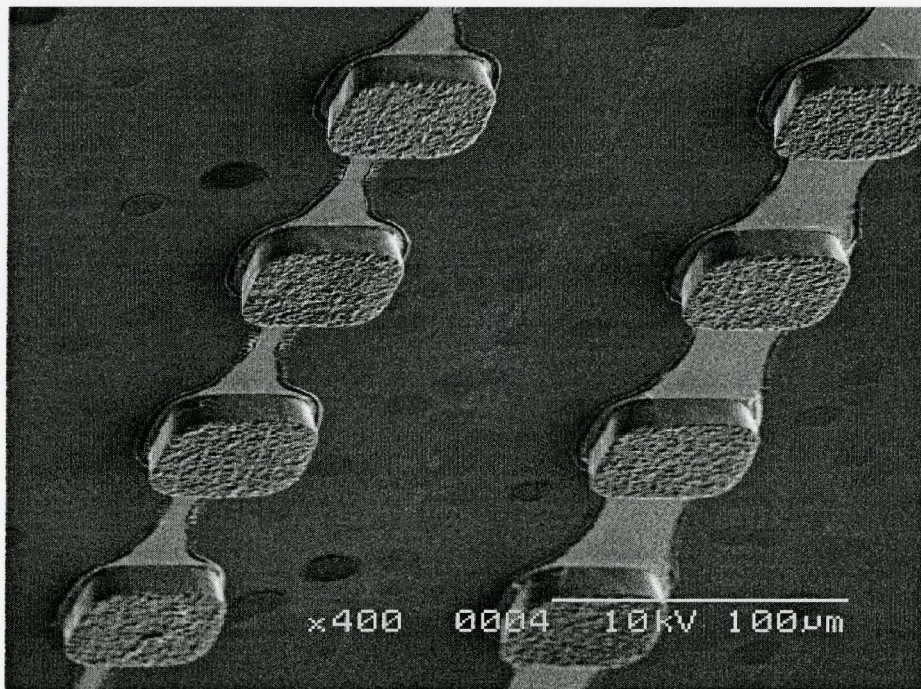Fig. 3.13 Typical nickel micropillar profile.

Fig. 3.14 SEM picture of 40 μm x 40 μm x 20 μm nickel micropillars.

In this work, nickel was electroplated to fabricate the micropillar electrodes. The electroplating solution (Ahn et al., 2005) used for this study is presented in Table 3.4. The sample was electroplated for 100 minutes at 10 mA/cm^2 in order to deposit 20 μm of nickel. A typical profile and SEM picture of 40 μm x 40 μm x 20 μm nickel micropillars are shown in Fig 3.13 and Fig. 3.14.

3.6 Summary

This chapter presents an overview of the different electrode designs used in this study. Four different planar and 3-D electrode configurations were developed. Critical design specifications are discussed and the details of the different micropump configurations are presented. The rational behind the selection of the electrode materials and working fluid are explained. Finally, the developed microfabrication process is presented along with advantages and limitations of each step of the procedure.

Chapter 4: Results and Discussion of EHD Micropump Characteristic

4.1 Introduction

This chapter presents and discusses the results of the EHD micropumps with HFE-7100 as the working fluid. The micropumps are tested under a no flow condition to measure the maximum pressure generation. The micropumps with planar and asymmetric planar electrode configuration were also studied for maximum flow rate under no imposed back pressure. Analysis of the effect of the different electrode configurations (i.e. planar electrode, asymmetric planar electrodes, 3D electrode, and asymmetric 3D electrode configuration) was performed. An explanation for the performance of the micropumps is provided by modeling the electric field within the pumps. The electric field was simulated for the different electrode geometries using a finite element method software (COMSOL Multiphysics). The effect of geometrical parameters, such as inter-electrode gap and micropillar separation distance, are investigated for the different electrode configurations.

4.2 Experimental Setup and Procedure

A Keithley 237 power supply was connected to the embedded emitter and collector electrode pads. The power supply had a maximum voltage output of 1100 V and a maximum current of 10 mA with a measurement uncertainty of 0.01 mV and 0.01 μA for voltage and current, respectively. Short glass tubings of 0.5 mm diameter were connected to the inlet and outlet of the micropump that functioned as the fluidic interconnections. Transparent plastic tubing of 1 mm diameter was subsequently connected to the glass tubings. For the static tests, the plastic tubings were positioned vertically as shown in Fig. 4.1. The micropump was filled with HFE-7100 using a syringe so that the fluid level could be easily detected in both the inlet and outlet
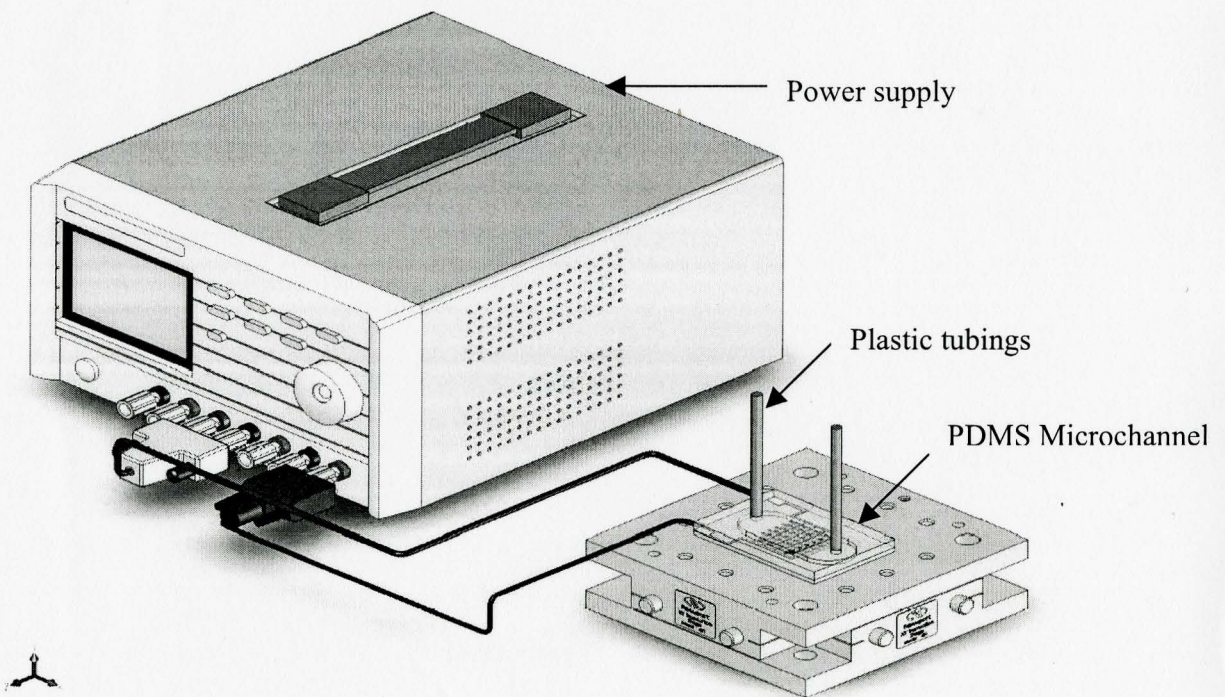

Fig. 4.1 Experimental setup for no-flow test.

51

columns to ensure no entrapped bubbles. The fluid level was checked to be equal before turning on the power supply. The pressure head was determined at different applied voltages by measuring the difference in the fluid level in the inlet and outlet columns using a height gage with a measurement uncertainty of ±0.1 mm. The uncertainty in the pressure measurement with HFE-7100 as the working fluid was ±2.8 Pa. The pressure generation voltage was increased in steps of 100 V.

For the flow tests, the inlet and outlet plastic tubing were positioned horizontally at the same level. The system was filled with HFE-7100 and a level was used to level the plastic tubings so that the fluid does not move due to any tubing inclination. A Fastec high speed digital camera with a capability of capturing 2000
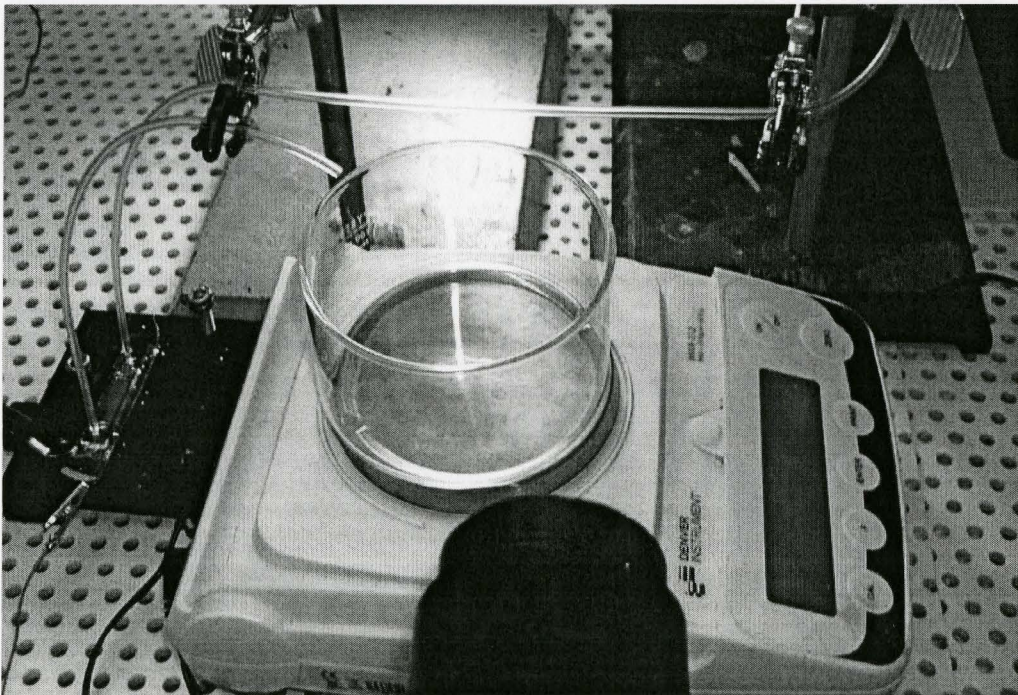

Fig. 4.2 Picture of experimental setup for flow test.

frames per second was used to image the moving liquid interface at the inlet plastic tubing. The velocity was estimated by measuring the displacement of the liquid interface over successive frames and the time between the frames using the motion measurement software provided by Fastec. The velocity measurement uncertainty was 0.2 mm/s. The volume flow rate was calculated using the measured liquid/air interface velocity and the plastic tubing area. A picture of the experimental setup for flow tests is shown in Fig. 4.2. Successive images showing the movement of liquid/air interface in the inlet plastic tubing is shown in Fig. 4.3.
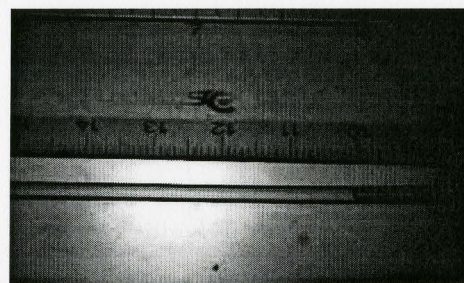
(a) t_1=0 sec
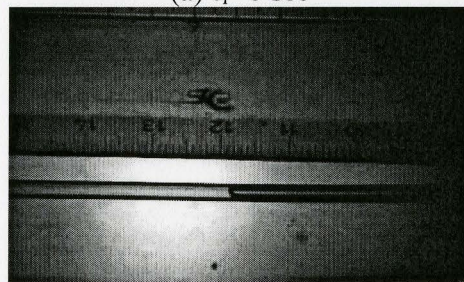
(b) t_2=12 sec
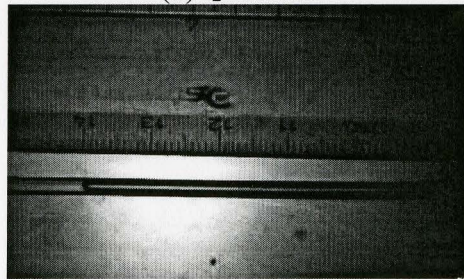
(c) t_3=28 sec

Fig. 4.3 Successive images showing the movements of liquid/air interface.

4.3 Numerical Modeling of Electric Field

To simulate the pumping phenomenon in EHD micropumps, the equations 2.5 – 2.11 have to be solved simultaneously for charge density distribution, electric potential, and fluid flow. Since the nature of charge injection at the emitter electrode in electrohydrodynamics is not fully understood, the proper boundary conditions for the charge density on the electrodes are unknown. Thus, it is not possible to obtain a solution with out a model for the charge boundary conditions at the electrodes. To obtain some insight into the behavior of the micropumps with different electrode configurations, the electric field was simulated numerically without coupling it to the fluid flow and electric charge distribution using COMSOL Multiphysics software. One pair of electrodes was modeled for each electrode configuration. The planar micropumps were modeled in both a 2-D cross section domain and a 3-D domain. The 3-D micropumps were modeled in a 3-D domain. The COMSOL Multiphysics electrostatic mode models the electrostatics of dielectric liquids which is governed by Eq. 2.5. The boundary conditions for the different walls are presented in Table 4.1

Table 4.1 Boundary conditions for electric field simulation.

Walls	Boundary conditions
Collector electrode	Ground (V=0)
Emitter electrode	Constant potential (V=500)
Other walls	Insulating wall ($\frac{\partial V}{\partial n} = 0$)

4.4 Results and discussion

The initial tests were performed under a no flow condition to estimate the maximum pressure generation of the micropumps. For consistency, all of the micropumps were 5mm wide with the height of the microchannel set at 100 μm. The inter-pair electrode spacing was two times the inter-electrode spacing. Each micropump had 100 pairs of electrodes and the microchannel length extended over the 100 pairs of electrodes. The geometrical specifications of the micropumps are given in Table 3.1 in Chapter 3. In the nomenclature of the micropumps, the number after "-S" designates the inter-electrode spacing in micrometers and the number after "-P" designates the distance between micropillars in the spanwise direction for the 3D electrode designs in micrometers. The prefix PE-, APE-, 3DE-, and 3DAE designate micropumps with symmetric planar electrode, asymmetric planar electrode, 3-D electrode, and 3-D asymmetric electrode configuration, respectively. For example, 3AD-S80-P120 refers to the micropump with 3D asymmetric electrode with inter-electrode spacing of 80 μm and distance between micropillars of 120 μm.

The effect of four different electrode configurations on the performance of the micropumps was investigated by testing four micropumps with identical inter-electrode spacing of 80 μm. The four micropumps tested were PE-S80, APE-S80, 3DE-P80-S80, and 3DAE-P160-S80. The current vs. voltage characteristics of these micropumps are presented in Fig. 4.4. The current increases exponentially as a function of voltage in all of the micropumps, and can be approximated as

$$I = C_1 . e^{(C_2 . V)} \qquad\qquad (4.1)$$

where C_1 and C_2 are constants. The increase in current with voltage is highest for the micropump with the 3D asymmetric electrode configuration (3DAE-P160-S80) with $C_2 = 0.0067$ and is lowest for the micropump with 3D symmetric electrode configuration (3DE-P80-S80) with $C_2 = 0.005$. The current is approximately equal for the planar electrodes (PE-S80) and asymmetric planar electrodes (APE-S80). In electrohydrodynamics, the charge injection is a function of the electric field gradient at the electrode liquid interface, which increases with a decrease of the radius of curvature of the electrode edges and a decrease of inter-electrode spacing. Since APE-S80 and PE-S80 have the same inter-electrode spacing with the same radius of curvature at the edges of the electrodes, it can be expected that both micropumps would have approximately equal current at a given applied voltage. The radius of
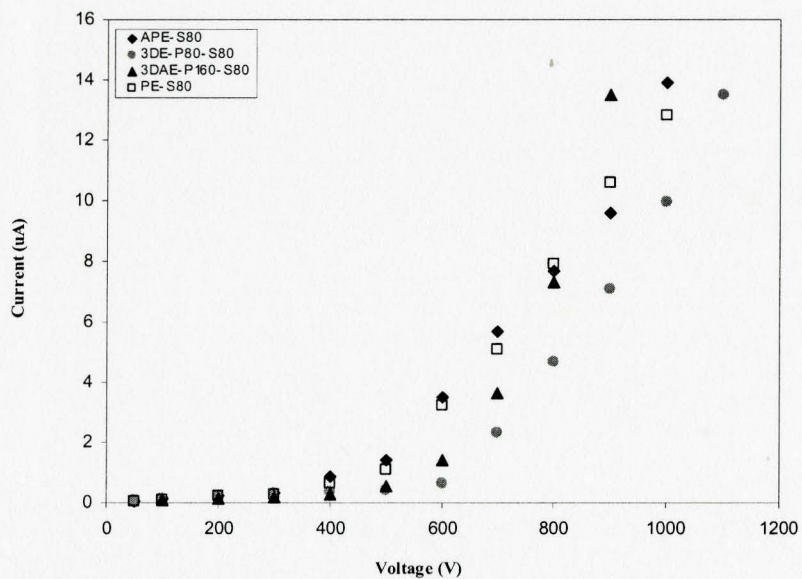

Fig. 4.4 Current vs. applied voltage for micropumps with different electrode configurations: APE-S80 with asymmetric planar electrodes, 3DE-P80-S80 with 3-D electrodes (micropillars/micropillars), 3DAE-P160-S80 with asymmetric 3-D electrodes (micropillars/flat), and PE-80 with symmetric planar electrodes.

curvature of the electrode edges for the planar electrodes is on the order of tenths of micrometers, which corresponds to the thickness of the gold electrode base. For the micropump with 3D symmetric electrodes, the radius of curvature of edges of the micropillars electrodes is on the order of several micrometers. Thus, the charge injection could be lower in this case and account for the higher current in micropumps with planar electrodes compared to 3DE-P80-S80. For 3DAE-P160-S80, the discharge characteristic are more complex since the emitter is composed of 3-D micropillars while the collector has planar electrodes. The 3DAE-P160-S80 has a higher current than 3DE-P80-S80 and the difference becomes more significant as the applied voltage increases above 600 V. The current in the 3DAE-P160-S80 is lower compared to both micropumps with the planar electrode configuration. Interestingly, the current in the 3DAE-P160-S80 micropump exceeds that of the APE-S80 and PE-S80 at applied voltages of 900 V.

The pressure generation under a no-flow condition for the four micropumps is plotted against the voltage and current in Fig. 4.5 and Fig. 4.6. The pressure increases exponentially with the applied voltage while it has a nearly linear relation to the current. The 3DAE-P160-S80 micropump generated the highest pressure head compared to the other micropumps, with a maximum pressure head of 2240 Pa at an applied voltage of 900 V. The micropumps with the asymmetric planar electrode configuration, APE-S80, generated a higher pressure head than 3DAE-P160-S80 at applied voltages lower than 600V which can be attributed to its the significantly higher discharge current compared to 3DAE-P160-S80 in this voltage range. At an

applied voltage of 600V, both micropumps generated pressure head of 290 Pa. As the applied voltage was increased beyond 600V, the pressure generation of 3DAE-P160-S80 surpassed that of APE-S80, which corresponds to the region where the current increased rapidly with voltage for the 3DAE-P160-S80. For example, at an applied voltage of 800 V, APE-S80 generated a pressure head of 720 Pa compared 1320 Pa for the 3DAE-P160-S80 micropump.

The APE-S80 micropump generates a higher pressure head compared to PE-S80. While the current vs. voltage characteristics indicates both micropumps have approximately similar discharge characteristic, the difference in the pump performance can be attributed to the differences in the electric field and charge density distribution within the pump. In order to reach a better understanding of the difference between the performances of these micropumps, the electric field within the pump domains was simulated numerically in the absence of the fluid flow and electric charge density distribution using COMSOL Multiphysics. Although neglecting the effect of the fluid flow and charge density distribution on the electric field and electric body force will provide results that are not conclusive, it provides an overview of the effect of different electrode geometries on the electric field distribution. The electric field vector diagrams for the planar and asymmetric planar electrode configuration are shown in Fig. 4.8 and Fig. 4.9. The integration of the electric field in the flow direction over the whole domain is two times more for the asymmetric planar electrode configuration compared to the planar symmetric electrode configuration.

The 3DE-P80-S80 generates a higher pressure head compared to the PE-S80. The electric field contours at the cross section of the 3DE-P80-S80 electrode configuratiion (Fig. 4.10) is more homogeneous compared with the 2D electric field contours for micropump PE-S80. By comparing the electric field component in the flow direction from the simulations, it can be concluded that the integration of the electric field in the flow direction over the domain of the micropump with 3-D electrode configuration is approximately 2.5 times higher than the micropump with symmetric planar electrodes. Therefore, despite its better discharged current, PE-S80 generates a lower pressure head compared to 3DE-P80-S80 because of the distribution of electric field in the flow direction. The electric field intensity is high near the bottom wall in the PE-S80 whereas in the 3DE-P80-S80 the electric field is more homogenous over the microchannel because of the micropillar electrodes. It was initially thought that the 3DE-P80-S80 would exhibit a better performance compared to both planar electrode configurations. However, the APE-S80 had a higher pressure generation compared to the 3DE-P80-S80 pump. Although the electric field in the flow direction of 3DE-P80-S80 is approximately 25% higher than the APE-S80, the discharge current of APE-S80 is two times higher at an applied voltage of 800 V. This results in a higher pressure head generation in APE-S80. However, the pressure head generation increases equally with respect to current for both micropumps. (Fig.4.6)
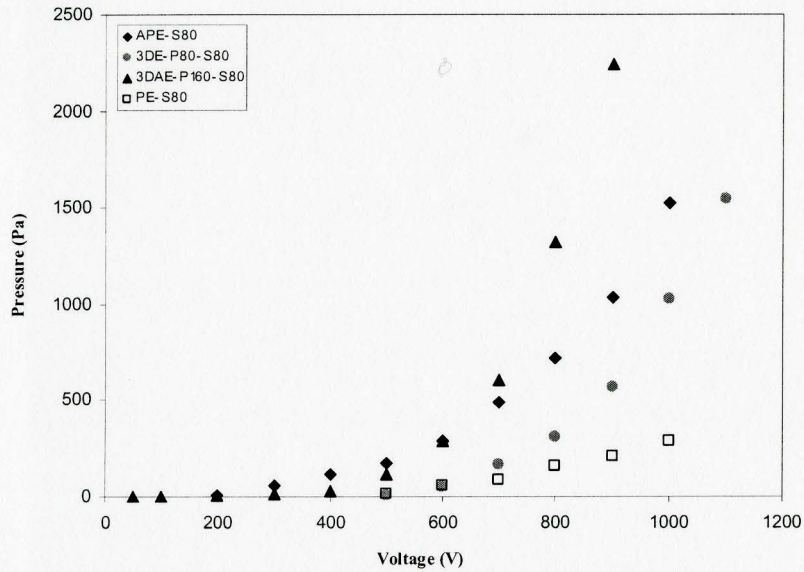
Fig. 4.5 Pressure vs. voltage for micropumps with different electrode configurations: APE-S80 with asymmetric planar electrodes, 3DE-P80-S80 with 3-D electrodes (micropillars/micropillars), 3DAE-P160-S80 with asymmetric 3-D electrodes (micropillars/flat), and PE-80 with symmetric planar electrodes.
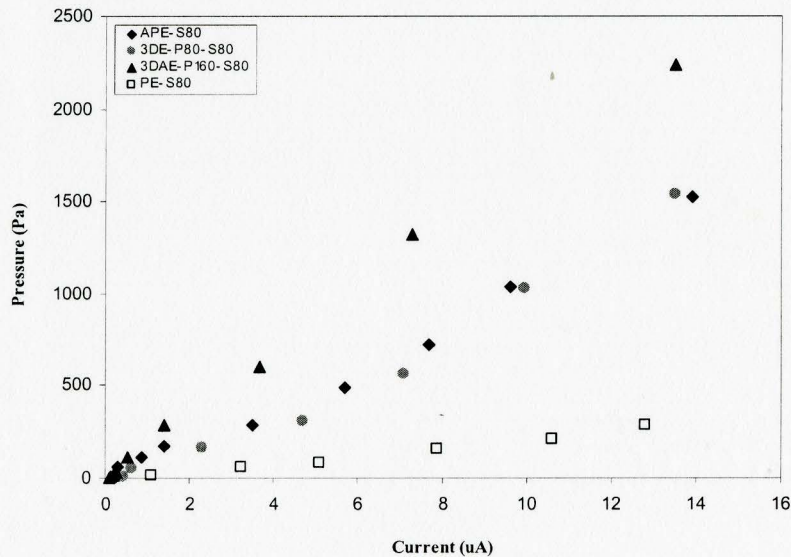

Fig. 4.6 Pressure vs. Current for micropumps with different electrodes configuration: APE-S80 with asymmetric planar electrodes, 3DE-P80-S80 with 3-D electrodes (micropillars/micropillars), 3DAE-P160-S80 with asymmetric 3-D electrodes (micropillars/flat), and PE-80 with symmetric planar electrodes.

The difference in the performance of the 3D-P80-S80 and 3AD-P160-S80 pumps is very interesting. The maximum pressure head generated by 3D-S80-P80 is 1540 Pa at an applied voltage of 1100 V while the maximum pressure head generated with 3AD-P160-S80 is 2240 Pa at an applied voltage of 900 V. The electric field in the Y direction in x-y and x-z cross sections of the microchannel for the micropumps with 3-D symmetric and 3-D asymmetric electrode configurations with inter electrode spacing of 80 μm are shown in Fig. 4.10 to Fig. 4.13. The integration of the electric field over the whole domain in the flow direction is approximately the same for both electrode configurations. The electric field intensity between the micropillars
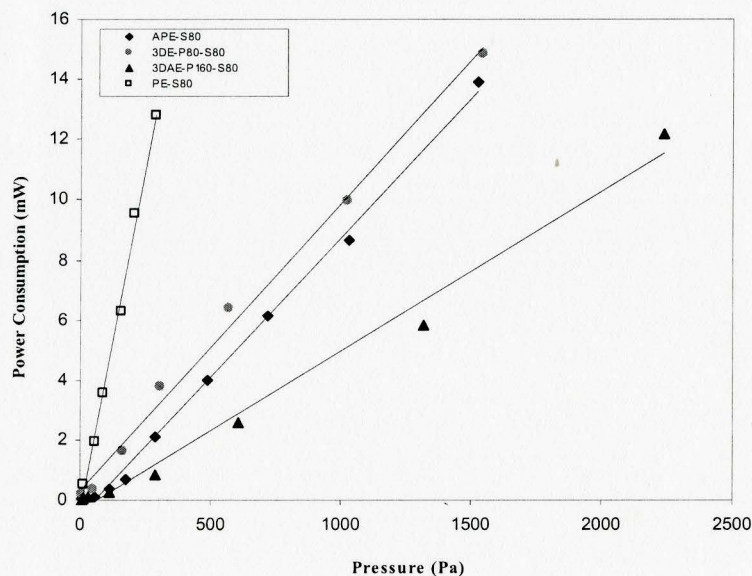

Fig. 4.7 Power consumption vs. pressure for micropumps with different electrodes configuration: APE-S80 with asymmetric planar electrodes, 3DE-P80-S80 with 3-D electrodes (micropillars/micropillars), 3DAE-P160-S80 with asymmetric 3-D electrodes (micropillars/flat), and PE-80 with symmetric planar electrodes.

contributes to the electric body force in the flow direction, but the collector micropillars act as obstacles to the fluid flow. Although in the steady state the net flow rate is zero, local flows and back flows are present in the microchannel. Therefore, the electrode geometry can result in internal loss and thus affect the pressure head. The micropump with the 3D asymmetric electrode configuration has a more homogeneous electric field in the flow direction over the microchannel and the collectors provide no blockage to the flow. The current-voltage characteristics show that this configuration has better discharge characteristics.

The power consumption for the four pumps as a function of pressure generation is shown in Fig.4.7. The power consumption is equal to current multiplied by voltage. The power consumption increases linearly with the pressure head generation. The 3DAE-P160-S80 has the least power consumption compared to the other electrode configurations for a given pressure generation. This can be attributed to its better discharge characteristics compared to 3DE-P80-S80 and more favorable electric field distribution compared to the PE-S80 and APE-S80 electrode configurations. For example, at a pressure head of 290 Pa, the power consumption of 3DAE-P160-S80, APE-S80, and 3DE-P80-S80 are 6.9%, 23.9%, and 31.1% of power consumption of the PE-S80, respectively. The power consumption of the PE-S80 is more than fifteen times the power consumption of 3DAE-P160-S80 for the same pressure generation. This suggests that, despite its acceptable discharge characteristic, the net electric body force vector is low in PE-S80 because of the electric field and charge distributions.
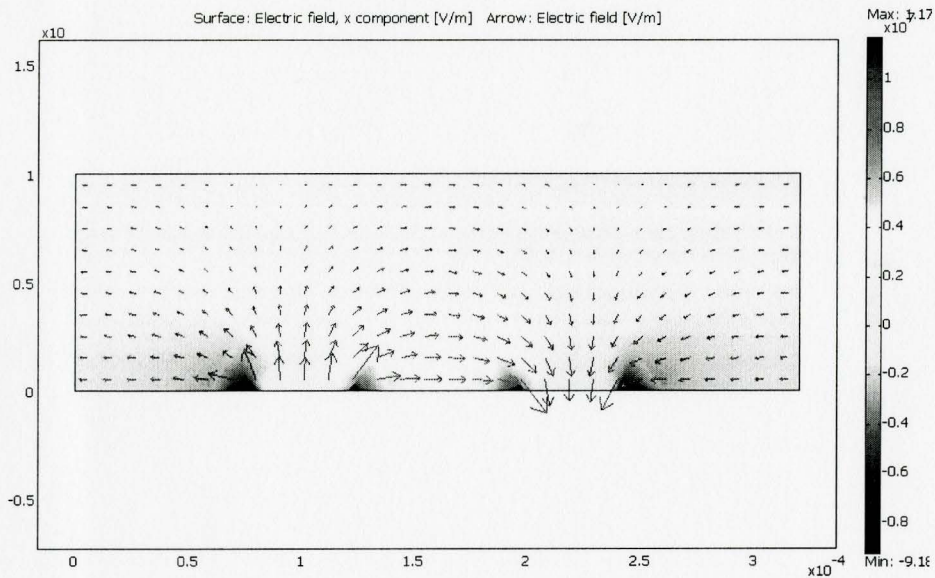
Fig. 4.8 Electric field vector for micropump with planar electrode configuration.
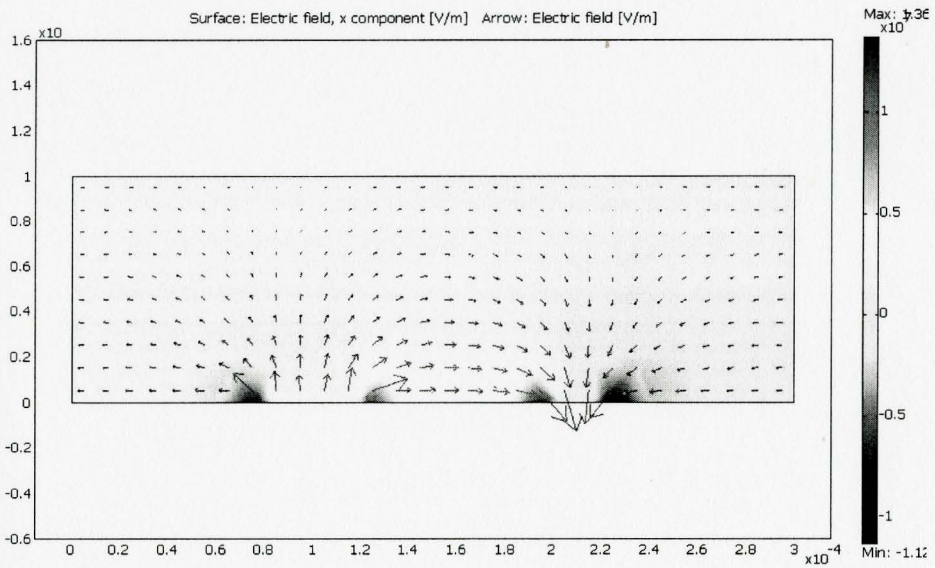
Fig. 4.9 Electric field vector for micropump with asymmetric planar electrode configuration.
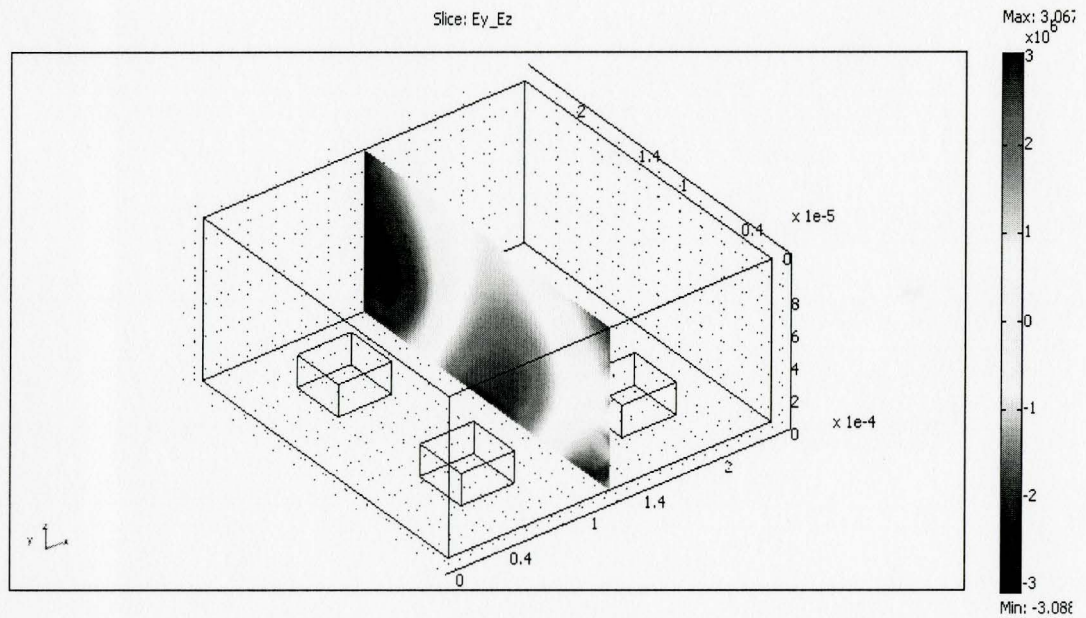
Fig. 4.10 Electric field in Y and Z direction contour in cross section between micropillars normal to Y direction for micropump with 3D electrode configuration. (Y is the flow direction)
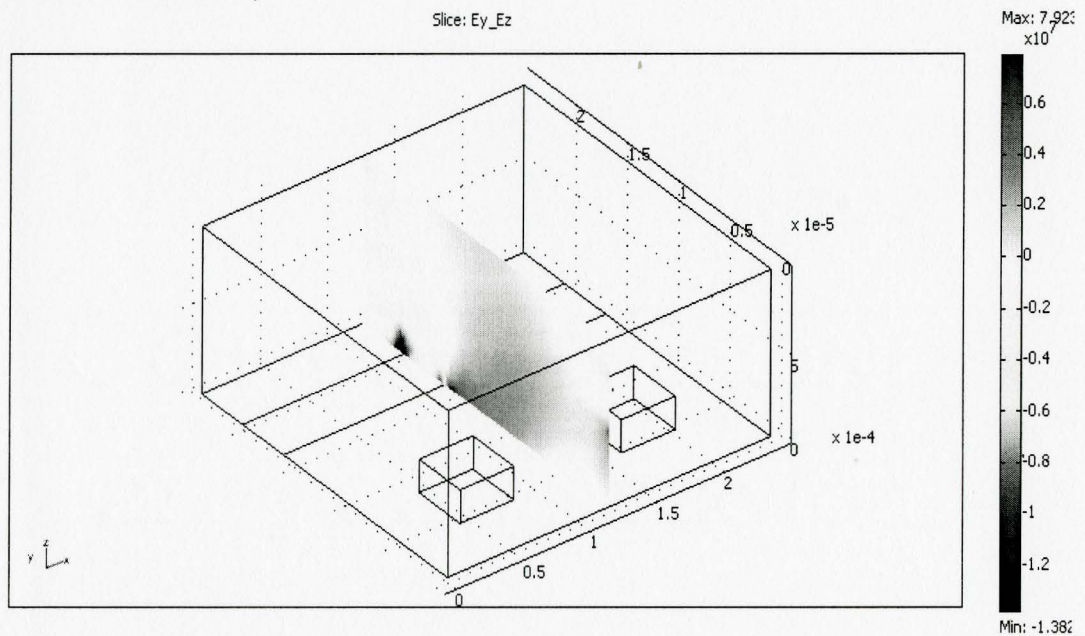

Fig. 4.11 Electric field in Y and Z direction contour in cross section between micropillars normal to Y direction for micropump with 3D asymmetric electrode configuration. (Y is the flow direction)
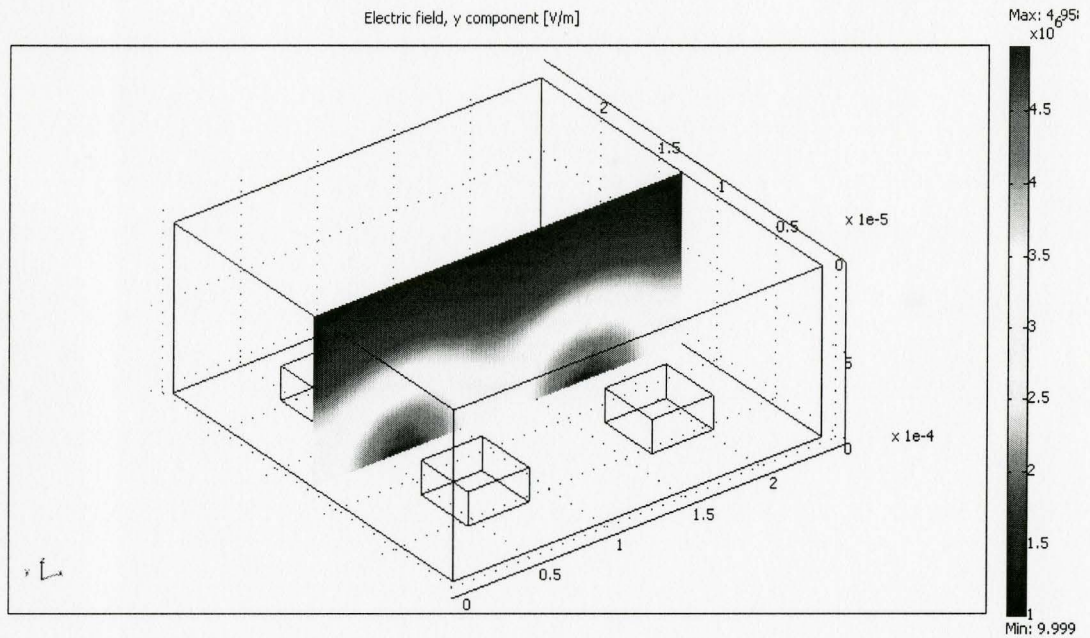
64

Fig. 4.12 Electric field in Y direction contour in cross section between micropillars normal to Y direction for micropump with 3D electrode configuration. (Y is the flow direction)
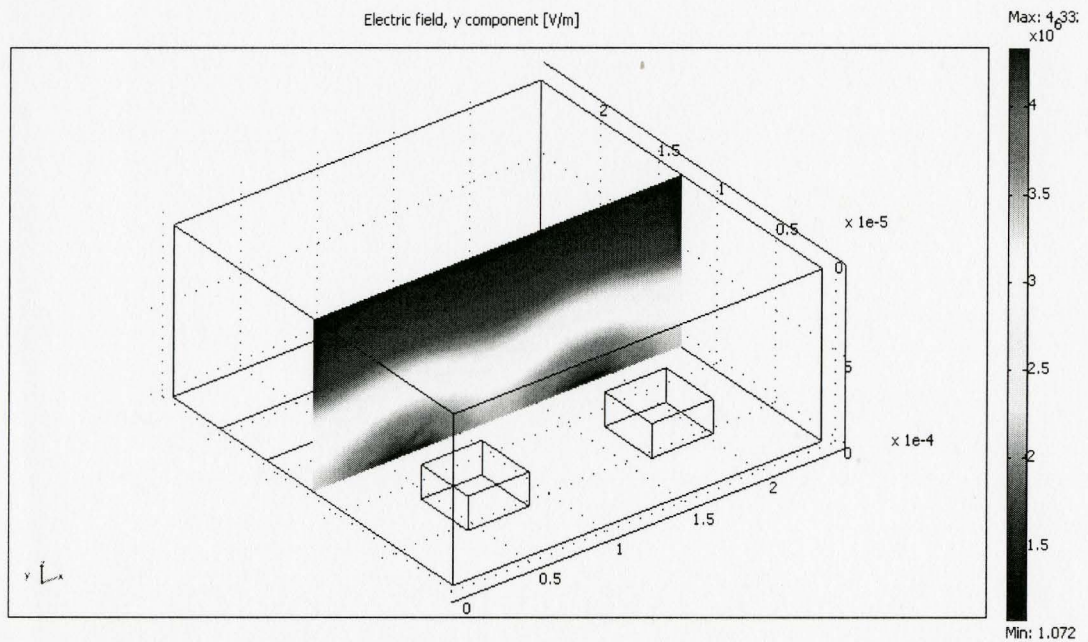

Fig. 4.13 Electric field in Y direction contour in cross section between micropillars normal to Y direction for micropump with 3D asymmetric electrode configuration. (Y is the flow direction)

The effect of inter-electrode spacing on the pump performance was investigated for planar, planar asymmetric and 3-D electrode configurations. The tests were performed for pumps with inter electrode spacing of 40 μm, 80 μm, and 120 μm. The current-voltage characteristics of these micropumps are shown in Fig. 4.13 to Fig. 4.15. The current increases exponentially with voltage for all micropumps, but as expected, the increase is more rapid as the inter-electrode spacing is decreased. In order to study the effect of the electric field on the discharge characteristic of these micropumps, the nominal electric field can be defined as

$$E_n = \frac{Applied voltage}{Interelectrode spacing}$$ (4.2)

For the APE-S40 at an applied voltage of 300 V or En of 7.5 V/μm the current is 3.6 μA. For the same nominal electric field the current for the micropumps with inter electrode spacing of 80 μm and 120 μm (i.e. at 600V in APE-S80 and at 900V in APE-S120), the current is 3.49 μA and 3.34 μA, respectively.

The dielectric breakdown is an uncontrolled avalanche of the charge passing trough the dielectric medium. The break down occurs when the electric field gradient exceeds a certain limit. Therefore, even though the charge injection is higher due to the higher electric field in the micropumps with smaller inter-electrode spacing, the break down occurs at a lower voltage. The maximum current for the micropumps with the same electrode configuration but different inter electrode spacing is approximately the same. For instance, break down occurs when the applied voltage exceeds 600V in APE-S40 with maximum current of 15.3 μA, and it occurs when the

applied voltage exceeds 1000V in APE-S40 with maximum current of 14.1 μA. Since the power supply had a highest voltage limit of 1100 V, break down was not reached in the PE-S120, APE-S120, 3DE-P80-S80, and 3DE-P80-S160 micropumps.

The pressure vs. voltage characteristics for the planar, planar asymmetric, and 3D electrode configuration with different inter electrode spacing are presented in Fig. 4.17, Fig. 4.18, and Fig. 4.19, respectively. The pressure head generation increases exponentially with voltage, similar to the current characteristics with voltage but with a higher growth rate. In the micropumps with smaller inter electrode spacing, the pressure head generation increases more rapidly with voltage. For example, the following trend lines can be fitted to the current vs. voltage and pressure vs. voltage characteristics for the APE-S120 micropump

$$I = C_1.e^{(0.0042V)} \tag{4.3}$$

$$P = C_2.e^{(0.006V)} \tag{4.4}$$

The pressure generation in these micropumps is mainly due to the Coulomb force generated within the flow domain as discussed previously. The current and consequently the charge density increase with electric field. Therefore, the electric body force, which is the product of the charge density and electric field, would increase at a higher rate than the current with respect to the applied voltage which results in a higher growth rate of pressure head generation compared to the current with respect to voltage. The pressure head is plotted against the electrode spacing for the different electrode configurations for a constant voltage in Fig.4.20. The pressure generation decreases with increase of inter electrode spacing for all three different

electrode configurations at a constant applied voltage. Since a higher pressure head can be generated at lower applied voltages by decreasing the inter electrode spacing, it is preferable to decrease the inter electrode spacing as far as manufacturing limits allows us.

The corresponding power consumption as a function of the pressure generation is presented in Fig. 4.21 to Fig. 4.23 for the different electrode configurations. These figures illustrate that a decrease of the inter-electrode spacing not only improves pressure generation but also reduces power consumption. The power consumption difference becomes more significant in higher pressure head generation. For example, APE-S80 generates 1034 Pa with power consumption of 8.64 mW whereas APE-S40 generates 1694 Pa at slightly higher power consumption of 9.2 mW. For micropumps with planar and 3-D symmetric electrode configuration, the power consumption is approximately equal for the micropumps with inter electrode spacing of 80 μm and 120 μm. The 3DE-P80-S40 and PE-S80 micropumps with inter electrode spacing of 40 μm have significantly lower power consumption per unit pressure head compared to their counterparts with inter electrode spacing of 80 μm and 120 μm.
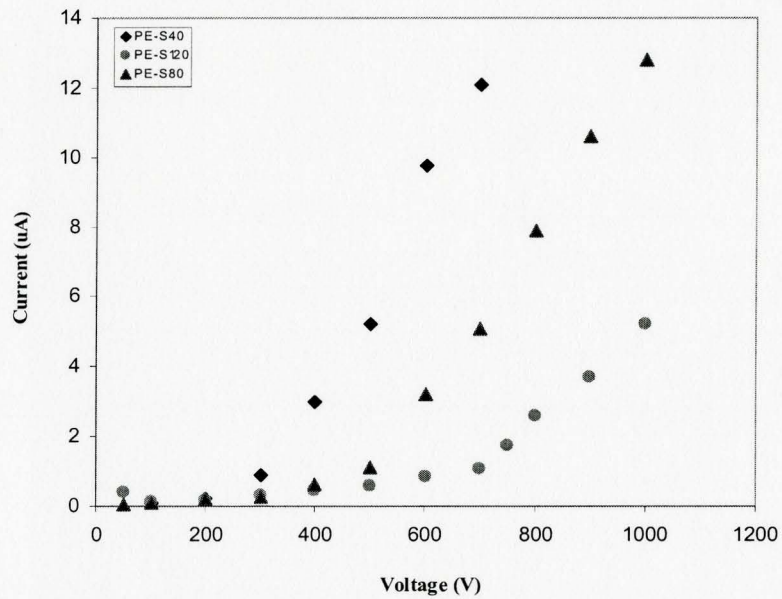
Fig. 4.14 Current vs. applied voltage for micropumps with planar electrodes with different inter-electrode gap.
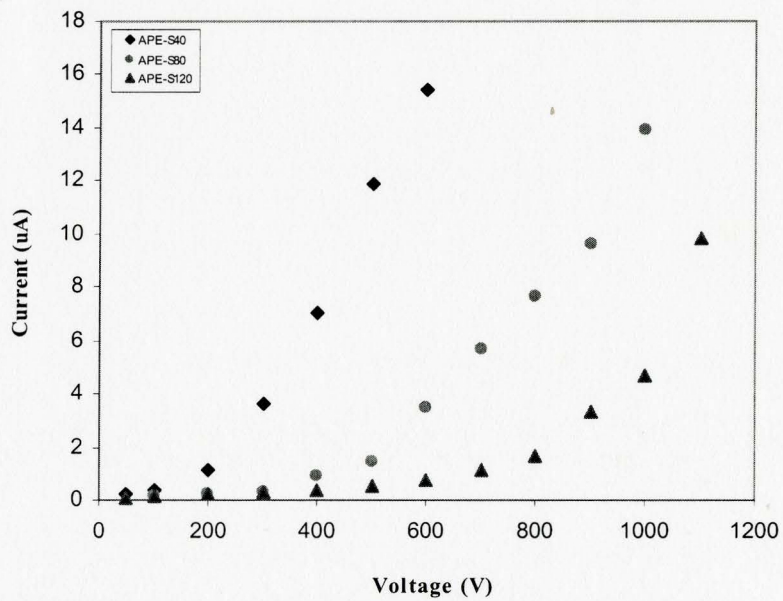

Fig. 4.15 Current vs. applied voltage for micropumps with asymmetric planar electrodes with different inter-electrode gap.

Fig. 4.16 Current vs. applied voltage for micropumps with 3-D electrodes (micropillars/micropillars) with different inter-electrode gaps.

Fig. 4.17 Pressure vs. applied voltage for micropumps with planar electrodes with different inter-electrode gap.
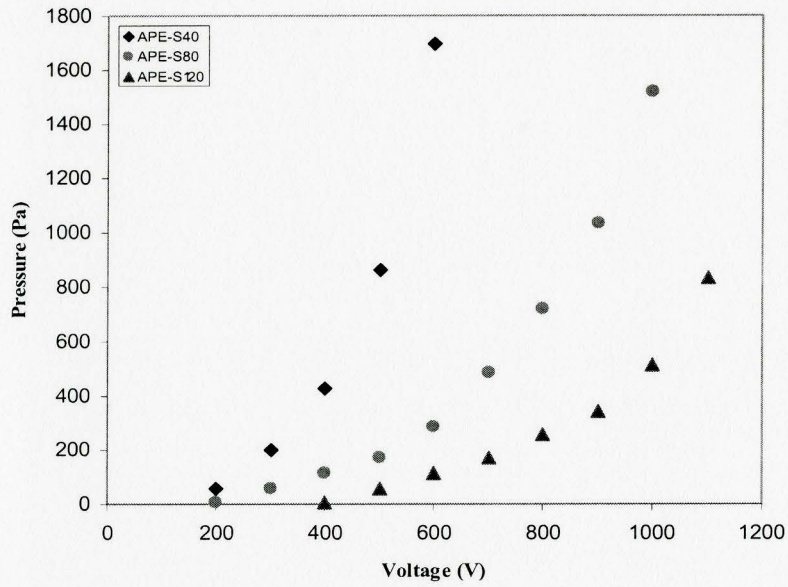
Fig. 4.18 Pressure vs. applied voltage for micropumps with asymmetric planar electrodes with different inter-electrode gap.
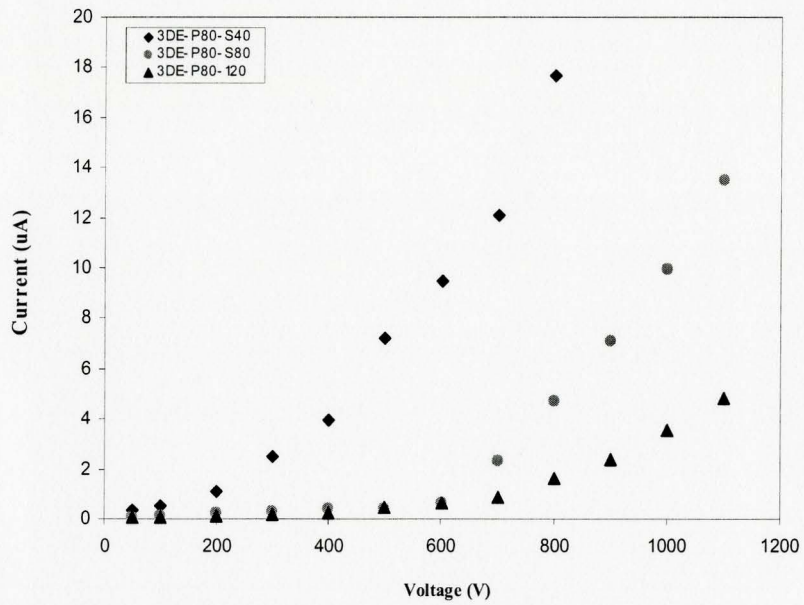

Fig. 4.19 Pressure vs. applied voltage for micropumps with 3-D electrodes (micropillars/micropillars) with different inter-electrode gap.
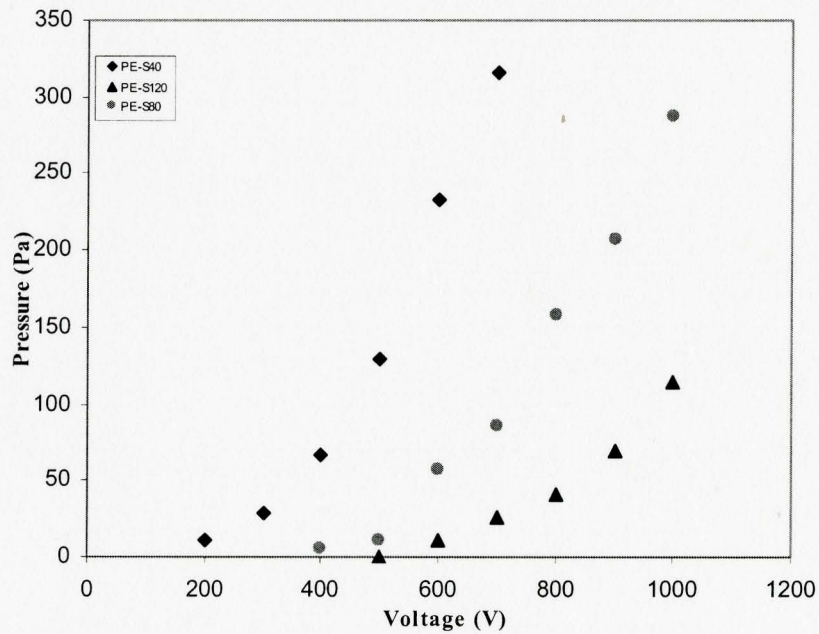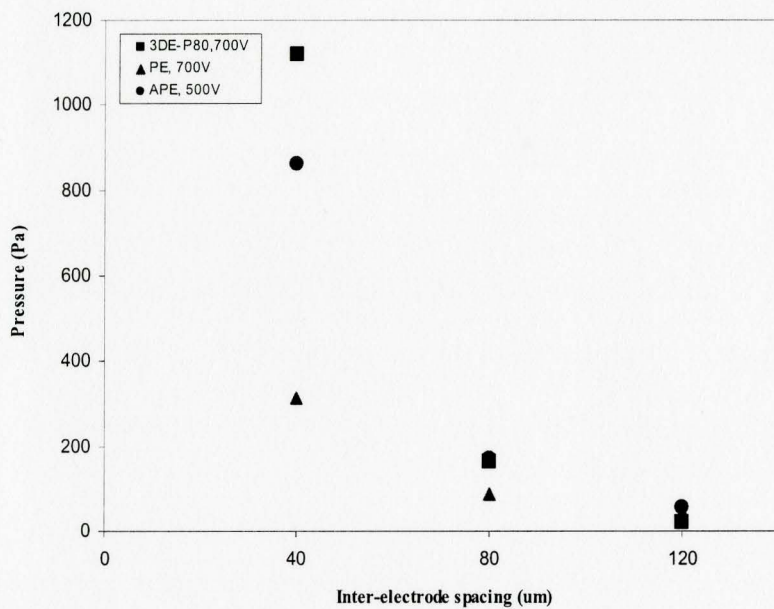
Fig. 4.20 Effect of inter-electrode gap on pressure generation in micropumps with different electrode configurations.
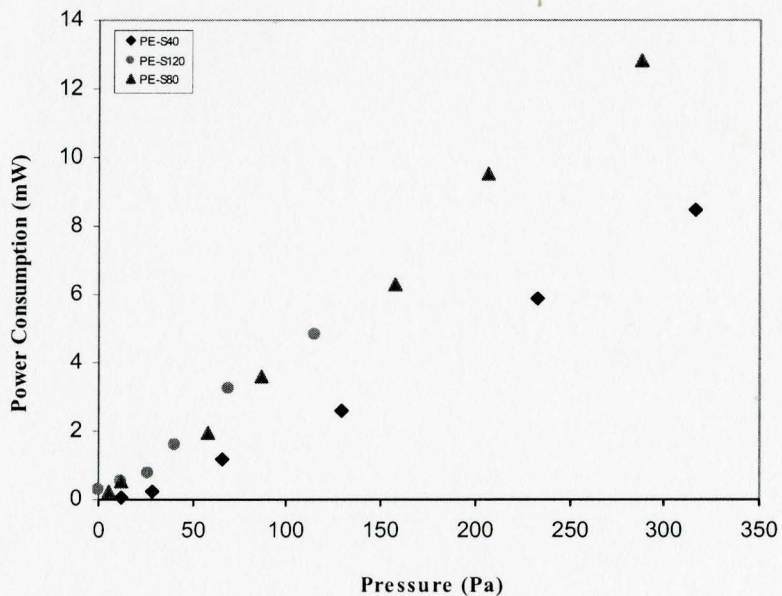
Fig. 4.21 Power consumption vs. pressure for micropumps with planar electrodes with different inter-electrode gap.
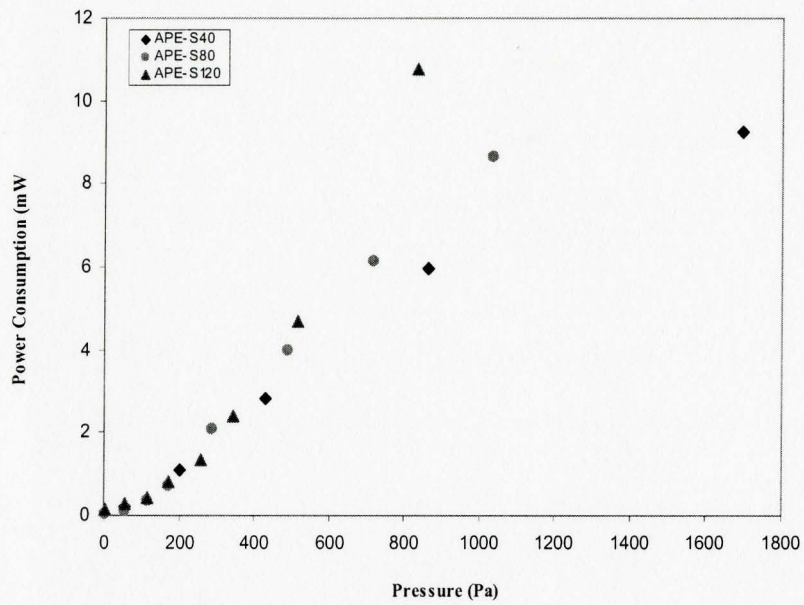
Fig. 4.22 Power consumption vs. pressure for micropumps with asymmetric planar electrodes with different inter-electrode gap.
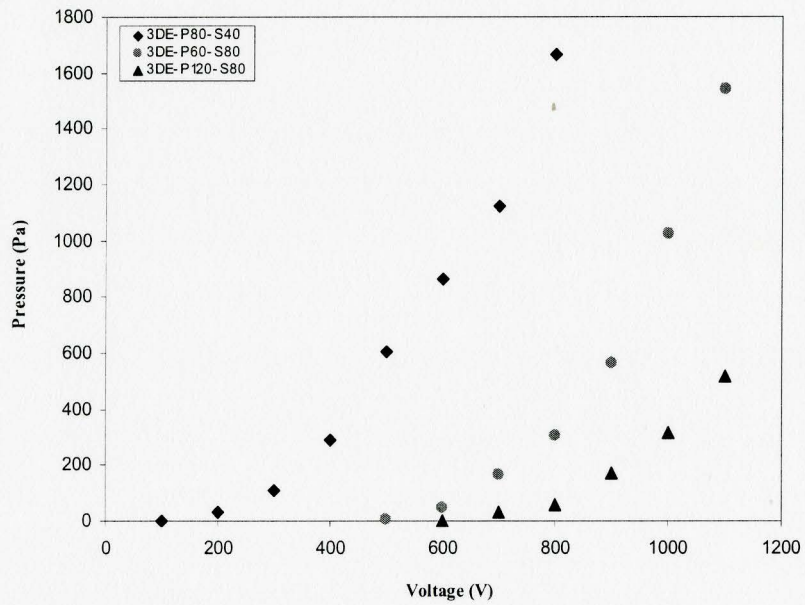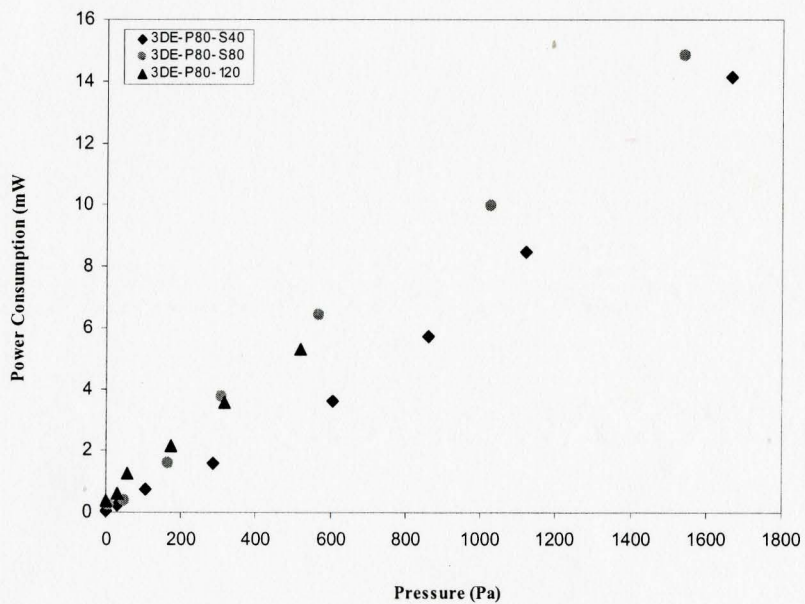

Fig. 4.23 Power consumption vs. pressure for micropumps with 3-D electrodes (micropillars/micropillars) with different inter-electrode gaps.

The effect of the pillar distance (i.e. the distance between the micropillars along the spanwise direction) on the pump performance was investigated for the 3D symmetric and asymmetric electrode configurations. The current-voltage characteristics for three different pillar distances of 40 μm, 80 μm, and 120 μm are shown in Fig.4.24 and Fig.4.25. Here, the inter electrode spacing was kept constant at 80 μm. The discharge characteristics of the micropump improves with a decrease of the micropillar distance for the micropumps with 3-D symmetric electrode configuration. This is expected since introducing more micropillars per unit length in the spanwise direction would increase the discharge. Surprisingly, the trend is opposite for the micropumps with the 3-D asymmetric electrode configuration. In this case, the discharge current is approximately equal at applied voltages lower than 600 V, but as the applied voltage increases beyond 600 V the micropump with a larger micropillar distance shows better discharge characteristics. At an applied voltage of 900 V, the current of the micropump with a micropillar distance of 160 μm is more than two times higher than the micropump with a micropillar distance of 80 μm. The reason for this is unclear at the time.

The pressure generation is plotted as a function of the applied voltage for the two micropump geometries with different pillar distance in Fig.4.26 and Fig.4.27. The pressure characteristic for both micropumps is similar to that of the current characteristic with respect to the micropillar distance. The pressure is plotted as a function of the micropillar distance in Fig. 4.28 and Fig. 4.29. For the 3D electrode

Fig. 4.24 Current vs. applied voltage for micropumps with 3-D electrodes (micropillars/micropillars) with different micropillars distances.
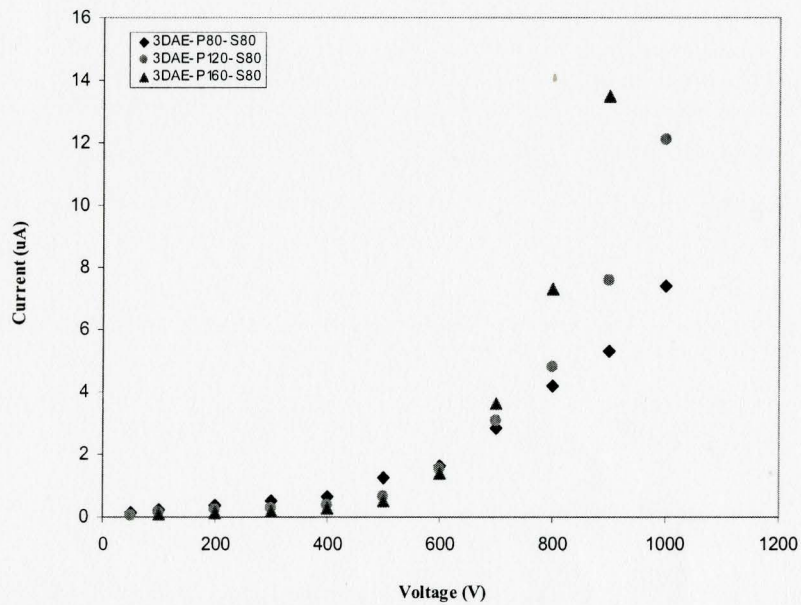

Fig. 4.25 Current vs. voltage for micropumps with 3-D asymmetric electrodes (micropillars/flat) with different micropillars distance.

Fig. 4.26 Pressure vs. applied voltage for micropumps with 3-D electrodes (micropillars/micropillars) with different micropillars distance.

Fig 4.27 Pressure vs. applied voltage for micropumps with 3-D asymmetric electrodes (micropillars/flat) with different micropillars distance.

Fig. 4.28 Effect of micropillars distance on pressure generation in micropumps with asymmetric 3-D electrodes (micropillars/flat).
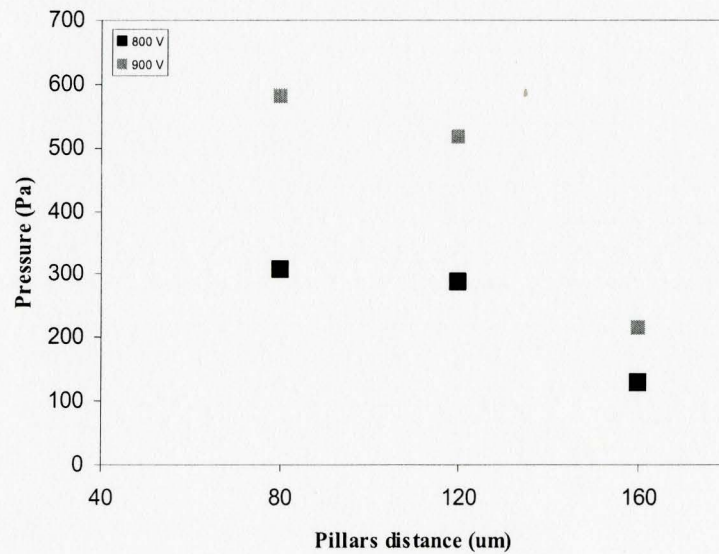
Fig. 4.29 Effect of micropillars distance on pressure generation in micropumps with 3-D electrodes (micropillars/micropillars).
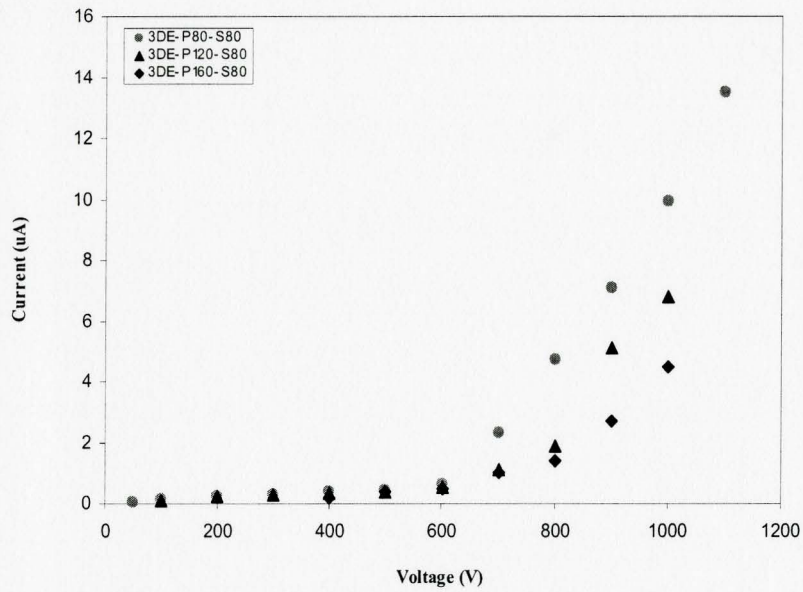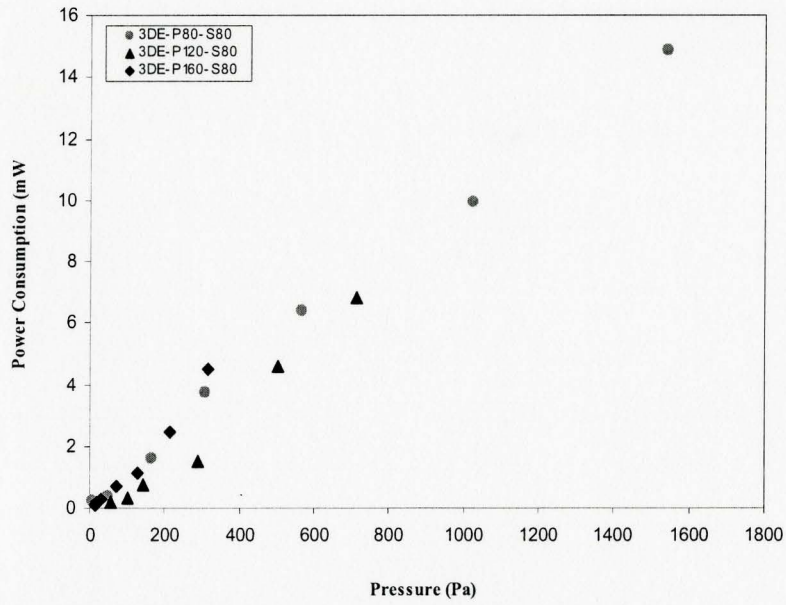
Fig. 4.30 Power consumption vs. pressure for micropumps with 3-D electrodes (micropillars/micropillars) with different micropillars distance.
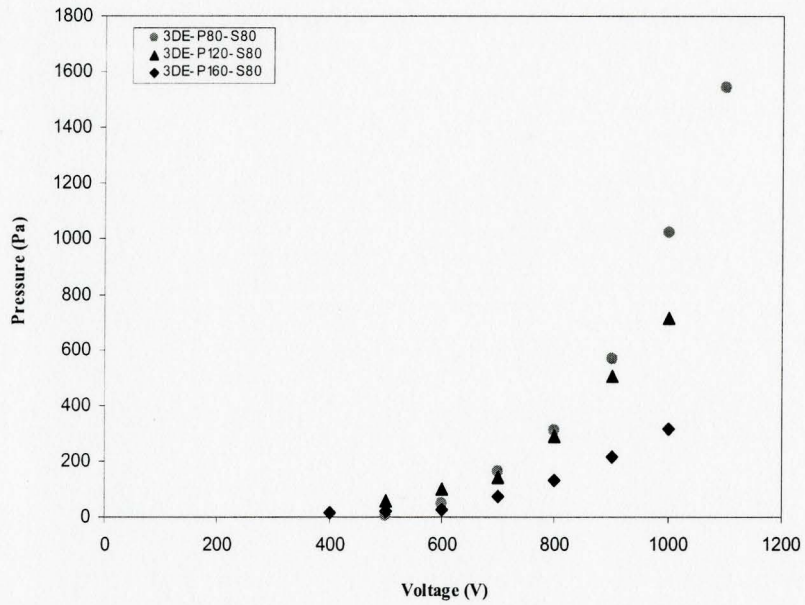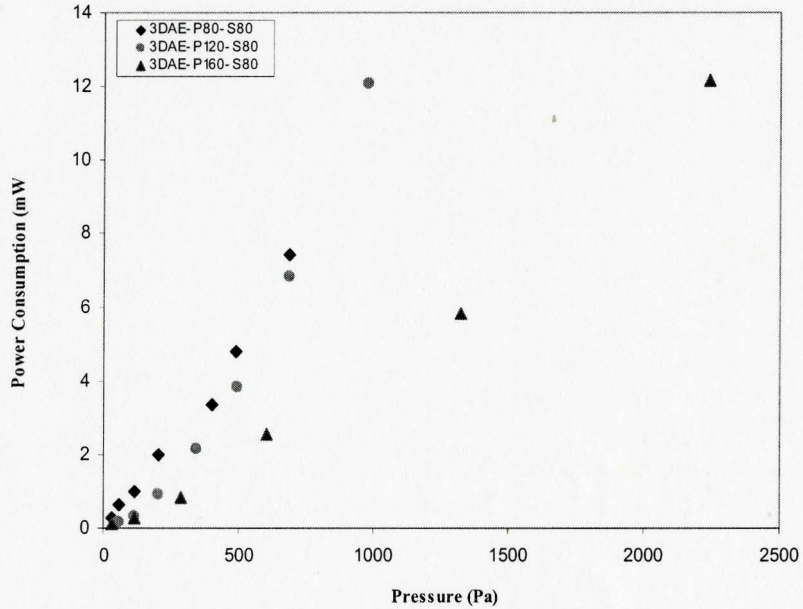

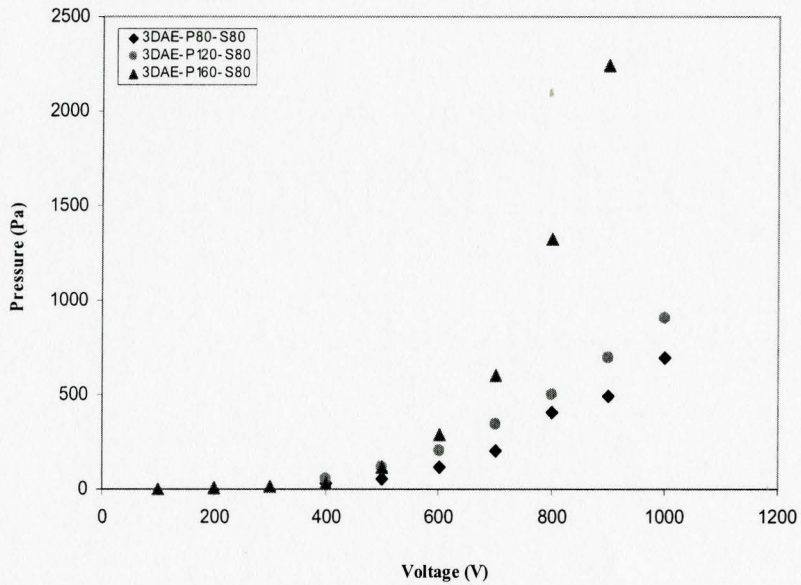Fig. 4.31 Power consumption vs. pressure for micropumps with 3-D asymmetric electrodes (micropillars/flat) with different micropillars distance.
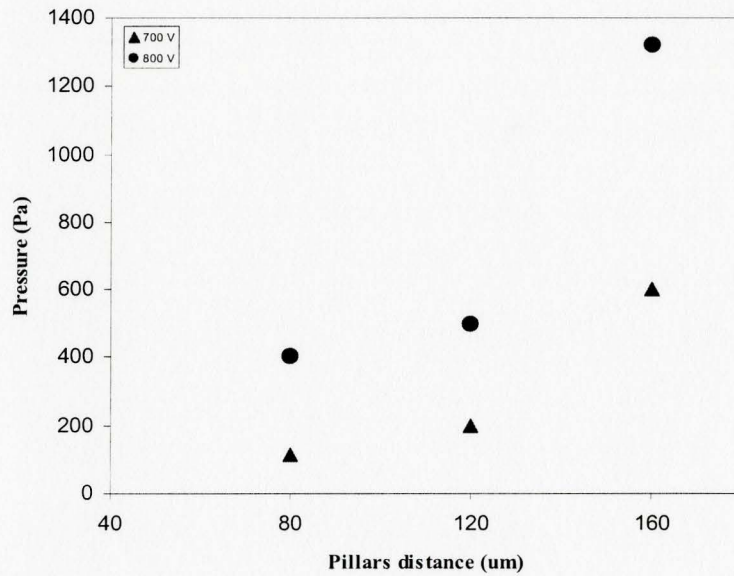
configuration, the pressure increases with a decrease of the micropillar distance, while for the 3D asymmetric electrode configuration the pressure decreases with a decrease of the micropillars distance. At an applied voltage of 800 V, the micropump with 3D symmetric electrode configuration and micropillar distance of 80 μm generated a pressure head of 580 Pa as this reduced to 215 Pa when the micropillar distance was increased to 160 μm. On the other hand, for the 3-D asymmetric electrode configuration, the micropump with micropillar distance of 160 μm and 80 μm generated a pressure head of 1320 Pa and 400 Pa, respectively. The power consumption is plotted against the pressure head for the 3-D electrode configuration with different micropillar distance in Fig. 4.30 and Fig. 4.31. The power consumption decreases with a decrease of micropillar distance for the micropumps with 3-D symmetric electrode configuration while it increases with a decrease of micropillar distance for the micropump with 3-D asymmetric electrode configuration distance, which is consistent with the current and pressure head generation characteristic.

The flow rate under a no back pressure condition for the PE-S80 and APE-S80 pumps are shown in Fig.4.32. The results shows that APE-S80 performs better under no back pressure condition and generates higher flow rates compare to the PE-S80 with symmetric planar electrode configuration. PE-S80 generated a maximum flow rate of 0.024 ml/min at an applied voltage of 900V, while the APE-S80 generated a maximum flow rate of 0.127 ml/min for the same applied voltage. The higher flow rate of PE-S80 can be attributed to the better distribution of the electric field compared to the APE-S80 with asymmetric electrode geometry.
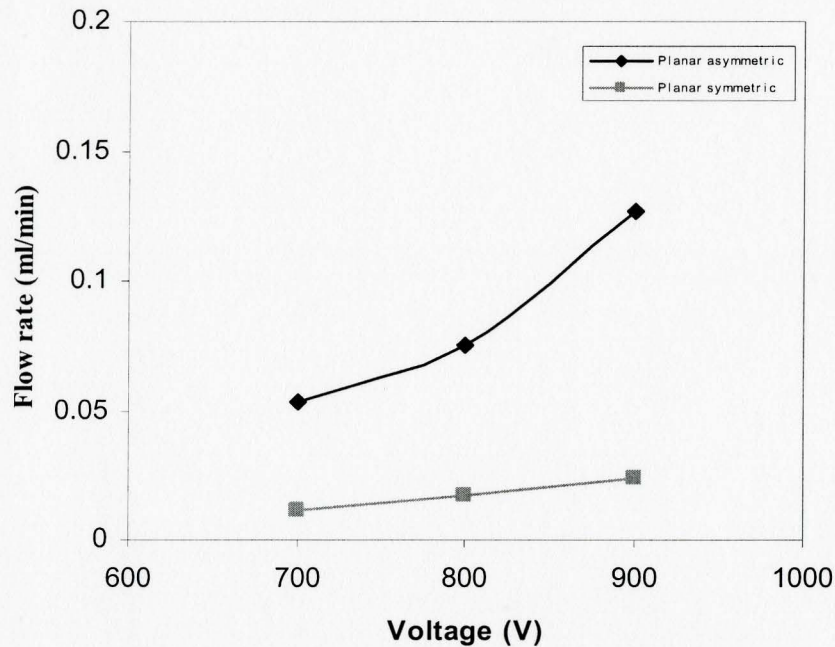
Fig. 4.32 Flow rate vs. voltage for micropump PE-S80 with planar electrode and micropump APE-S80 with asymmetric planar electrode configuration.

The electric field simulation shows that the integral of the electric field of the micropump with planar asymmetric electrode configuration in the flow direction over the whole domain is nearly two times higher than that of the micropump with planar symmetric electrode configuration, which would result in a higher electric body force. Since APE-S80 generates a higher pressure under a no flow condition and higher flow rate under a no back pressure condition than that of PE-S80, it can be concluded that micropumps with asymmetric planar electrode configuration have a better overall performance.

4.5 Summary

An experimental study was conducted to investigate the effect of different electrode geometries on the performance of EHD micropumps. The tests were performed for both a no flow condition to determine the maximum pressure generation and flow tests under no imposed back pressure. Fourteen different micropumps were tested with HFE-7100 as the working fluid. The effect of the different electrode configuration on the micropump performance are presented and discussed. The micropump with 3-D asymmetric electrode configuration showed the highest performance compared to micropumps with other electrode configurations. The 3DAE-P160-S80 generated a maximum pressure head of 2240 Pa an applied voltage of 900V. The effect of the inter-electrode spacing and micropillars distance was investigated for different electrodes configuration. The results show that a decrease in inter electrode spacing leads to higher pressure head generation and lower power consumption at a certain applied voltage. Micropumps with symmetric and asymmetric electrode planar were tested under no back pressure condition. The micropump with asymmetric planar electrode configuration generated higher flow rate compared to the micropump with symmetric planar electrode configuration.

Chapter 5: Conclusion and Recommendations for Future Works

5.1 Introduction

This chapter presents a summary of the accomplishments of this study. The key challenges of the research are reviewed, and the solutions that were implemented are presented. The conclusion section summarizes the experimental results of the micropumps with different electrode configurations and different configuration specifications. During the course of the present investigation several new characteristics of the EHD micropumps have been identified that should be explored. Future research is needed to fully understand the effect of each configuration factor in order to give us a more complete understanding of this complicated phenomenon. This chapter concludes with recommendations for future work in order to clarify some of the questions which have arisen in the present work.

5.2 Overview and Conclusions

The objective of the present study was to investigate the effect of different electrode geometry configurations and design specification, such as inter electrode spacing and distance between micropillars in the spanwise direction, on the performance of EHD micropumps. Four different electrode configurations were investigated: (1) Planar symmetric, (2) Planar asymmetric, (3) 3-D symmetric, and (4) 3-D asymmetric. In the planar symmetric electrode (PE) configuration, the width of both the emitter and collector electrodes is equal to 40 μm whereas in the asymmetric planar electrode (APE) configuration the width of the collector electrodes are half the width of the emitter. The 3-D symmetric electrode (3DE) configuration consisted of micropillar emitter and collector electrodes whereas the 3D asymmetric electrode (3DAE) configuration consisted of micropillar emitter electrodes and flat collector electrodes. Fourteen micropumps with different electrode configuration and different geometry specifications were manufactured.

The microfabrication protocols and procedure were developed for the EHD micropumps. The electrodes were fabricated using a two mask process. First, a thin layer of chromium was deposited on glass as a seed layer for gold electrode. Positive photoresist (AZ P4620) was patterned to form the mould for the micropillars. Nickel was electroplated to fill the mold. Subsequently, Cr/Au layer was patterned to devise the electrode base connector and pads. The microfluidic channels were fabricated by casting polydimethylsiloxane (PDMS) on top of an SU-8 100 (MicroChem Corp.) mould which was patterned to delineate the microchannel structure. The PDMS

microchannel was integrated on the electrode part by plasma oxidizing PDMS and glass wafer and sealing the connection with liquid PDMS as glue.

Fabrication of the high aspect ratio micropillars for the micropumps with 3-D electrode configurations was one of the key challenges faced in the fabrication process. Here nickel micropillars were fabricated using electroplating technique. A commercial electroplating solution (Alfa Aesar bright and finished nickel plating solution) and a electroplating solution suggested by Ahn et al. were characterized at different current densities. It was found that plasma oxidizing of the wafer before the electroplating process and maintaining the electroplating solution temperature at 50 °C had a significant effect on the quality and uniformity of the electroplating. PDMS bonds easily with glass using plasma oxidization technique, however, it does not bond with gold at all. The problem with the conventional stamping technique was that the PDMS liquid flowed and clogged the microchannel. In the current process, the sample and PDMS microchannel were plasma oxidized, aligned and assembled. Then, the sample was heated up to 150 °C and 1:3 curing agent to liquid PDMS mixture was poured at the boundary of the microchannel as sealing glue. The high temperature accelerated the curing process of the liquid PDMS and prevented it from blocking the microchannel.

The micropumps were tested under a no net flow condition with HFE-7100 as the working fluid. Two planar micropumps were tested for flow under a no back pressure condition. The results from this study are summarized as follows:

- The micropumps with 3D asymmetric electrodes generated a higher pressure and consume lower power per unit pressure compared to the micropumps with the other electrode configurations and same inter electrode spacing. The micropump 3DAE-S80-P160 generated the highest pressure head of 2240 Pa at an applied voltage of 900V.

- The micropumps with asymmetric electrode geometry, in both planar and 3-D electrode configurations, had a better performance compared to their counterpart with symmetric electrode geometry.

- The discharge characteristics of the planar micropumps with symmetric and asymmetric electrode geometry with equal inter electrode spacing are approximately similar. This can be attributed to the equal radius of curvature and shape of the electrode edges which results in similar electric field intensity and gradient.

- The current increases exponentially with respect to applied voltage for all micropumps. The growth rate is higher for the micropumps with lower inter electrode spacing. The discharge current of the micropumps with certain electrode configuration increases with the nominal electric field, which is function of the potential divided by the inter electrode spacing.

- The pressure head increases exponentially with applied voltage, while it is approximately linear with respect to the current.

- The pressure generation increases and power consumption decreases with the decrease of the inter electrode spacing.

- In the micropumps with 3D symmetric electrode configuration, the pump performance increases with decrease of the micropillars distance whereas in the micropumps with 3D asymmetric electrode the pump performance decreases with increase of the micropillar distance.

- The micropump with planar asymmetric electrode configuration generated a higher flow rate compared to the micropump with planar symmetric electrode configuration under a no back pressure condition. This result was corroborated from the numerical simulation of the electric field, which shows that the integration of electric field with the planar asymmetric electrode configuration is two times higher than that of the micropump with planar symmetric electrode configuration with identical inter electrode spacing.

5.2 Recommendation

More research has to be done in order to fully investigate the effect of the various electrode configurations and working fluid on the performance of the EHD micropumps. The following are recommended for future research:

- Measuring the flow using a PIV system can shed light on the flow field in the micropump with different electrode configuration, which can be helpful to optimize the micropump design.

- Fabricate and test micropumps with 3-D asymmetric electrode and higher micropillars distance in order to completely study the effect of the micropillars distance on the pump performance.

- Investigate the effect of the different working fluids and additives on the pump performance and discharge characteristics.

- Develop micropumps in which the electrode edges are covered by a layer of insulating material so that the effect of the EHD conduction pumping can be evaluated in the micropumps.

REFERENCES

Ahn, S., and Kim, Y.K., (1998). "Fabrication and experiment of a planar micro ion drag pump." Sensors and Actuators A, 70:1-5

Asano, K., and Yatsuzuka, K. (1999). "Fundamental study of EHD pump with needle cylinder electrodes." Conference on Electrical Insulation and Dielectric Phenomena, Piscataway, NJ, USA.

Atten, P., and Seyed-Yagoobi, J. (1999). "Electrohydrodynamically Induced Dielectric Liquid Flow Through Pure Conduction in Point/Plane Geometry - Experimental Study." , Proceedings of 13'h International Conference on Dielectric Liquids (ICDL '99), Nm, Japan.

Atten, P., Seyed-Yagoobi, J., and Jeong, S. (2003). "Electrohydrodynamically induced dielectric liquid flow through pure conduction in point/plane geometry." IEEE Trans. Dielectr. Electr. Insul., 10: 27–36.

Bart, S. F., and Tavrow, L.S. (1990). "Microfabricated Electrohydrodynamic Pumps." Sensors and Actuators, A: Physical, 21:193-197.

Benetis, V., Shooshtari, A., Foroughi, P., and Ohadi, M (2003)."A Source-Integrated Micropump For Cooling of High Heat Flux Electronics." 19th IEEE SEMI-THERM Syposiom.

Benetis, V. (2005). "Experimental and compoutational investigation of planar ion drag micropump geometrical design parameters." PHD Thesis, Mechanical Engineering, College park, University of Maryland.

Bologa, M. K., and I. A. Kozhukhar (1993). "Electrohydrodynamic pump service life." IEEE 11th International Conference on Conduction and Breakdown in Dielectric Liquids, Piscataway, NJ, USA.

Brand, K., and Seyed-Yagoobi, J. (2003). "Experimental study of electrohydrodynamic induction pumping of a dielectric micro liquid film in external horizontal condensation process." ASME J. Heat Transfer, 125: 1096–1105.

Bryan, J.E. (1990). "An Experimental Study of Ion-drag Pumping in a Vertical Axisymmetric Configuration." Master's Thesis, Texas A&M University, College Station, TX

Bryan, J. E., and Seyed-Yagoobi, J. (1991). "Experimental study of ion-drag pumping using various working fluid." IEEE transaction on electrical insulation, 26: 647-655

Bryan, J.E., and Seyed-Yagoobi, J. (1992). "An experimental investigation of ion-drag pump in a vertical and axisymmetric configuration." IEEE Trans. Ind. Appl., 28: 310–316.

Castaneda, J. A., and Seyed-Yagoobi, J. (1991). "Electrohydrodynamic pumping of refrigerant 11." IEEE Industry Applications Society Annual Meeting, 1: 500-505

Chang, J.S., Lawless, P.A., and Yamamoto, T. (1991). "Corona discharge Process." IEEE Transacion on Plasma Science, 19(6): 1152-1166

:

Chang, J.S., Ohyama, R., and Watson, A. (2001)." Electrical current conduction and electrohydrodynamically induced fluid flow in an AW type EHD pump." Journal of Electrostatics, 53 : 147–158

Coletti, G., and R. Bozzo (1996). "A contribution to the evaluation of electrohydrodynamic pumps for insulating oils." IEEE 1996 Annual Report of the Conference on Electrical Insulation and Dielectric Phenomena, New York, NY, USA.

Crowley, J. M., and Wright, G.S. (1990). "Selecting a Working Fluid to Increase the Efficiency and Flow-Rate of an Ehd Pump.", IEEE Trans. on Industry Applications, 26: 42-49.

Chattock, A. P., and Walker, W.E. (1901). Philosophical Magazine, 1: 79-85.

Darabi, J., Ohadi, M., and DeVoe, D. (2001). "An Electrohydrodynamic Polarization Micropump for Electronic Cooling." J. Microelectromechanical Systems, 10(1): 98-106

Darabi, J., Rada, M., Ohadi, M., and Lawler, J. (2002). "Design, Fabrication, and Testing of an Electrohydrodynamic Ion-Drag Micropump." J. Microelectro-mechanical systems, 11(6): 684-690

Darabi, J, and Wang, H. (2005)." Development of an Electrohydrodynamic Injection Micropump and Its Potential Application in Pumping Fluids in Cryogenic Cooling Systems." J. Microelectro-mechanical systems, 14(4): 747-755

Feng, Y., and Seyed-Yagoobi, J. (2004). "Understanding of electrohydrodynamics conduction pumping phenomenon.", J. Phys. Fluids, 16: 2432–2441.

Feng, Y., and Seyed-Yagoobi, J. (2007). "Electrical Charge Transport and Energy conversion with Fluid Flow During Electrohydrodynamic Conduction Pumping.", J. Phys. Fluids, in press.

Foroughi, P., Benetis, V., Ohadi, M., Zhao, Y., and Lawler, J. (2005). "Design, Testing and Optimization of a Micropump for Cryogenic Spot Cooling Applications." 21st annual IEE Semiconductor Thermal Measurement and Management Symposium.

Fowler, R. H. (1928). "The restored electron theory of metals and thermionic formulae." Royal Society Proceedings, 117(A778): 549-552.

Jang, J., and Lee, S.S. (2000)."Theoretical and experimental study of MHD (magnetohydrodynamic) micropump." Sensors and Actuators, A 80: 84–89.

Jinag, L., Wong, M., and Zohar, Y. (2001). "Forced convection boiling in a microchannel heat sink.", J. Microelectromechanical Systems,10(1): 80-87.

Jeong, S., and Seyed-Yagoobi, J. (2004). "Innovative Electrode Designs for Electrohydrodynamic Conduction Pumping." IEEE Trans. On Industry Applications, 10(3): 900-904.

Jun, T.K., and Kim, C.J. (1996). "Microscale pumping using traversing vapor bubbles in microchannels." *Solid-State Sensor and Actuator Workshop*, Hilton Head, South Carolina:144–147.

Kano, I., and Takhashi, I. (2006). "Improvement of pressure performance of Micro-EHD pump with an arrangement of thin cylindrical electrodes." JSME international journal, Series B, 149(3): 748-754

Lee, J., and Kim, C.J. (2000). "Surface-tension-driven microactuation based on continuous electrowetting." *J. Microelectromech. Syst.,* **9**: 171–180.

Malakhov, A.V. (1999). "The Effect of Time Factor upon the Stability of Output Parameters of Electrohydrodynamic Converters." Proceedings of 13th International Conference on Dielectric Liquids (ICDL '99), Nara Japan: 20-25

Melcher J.R. (1966). "Traveling-wave induced electro-convection.", Phys. Fluids, 9: 1548–1555

Melcher, J. R., and Firebaug, M. (1967). "Traveling-Wave Bulk Electroconvection Induced across a Temperature Gradient." Physics of Fluids, **10**(6): 1178-1186.

Pickard, W. F. (1963). "Ion Drag Pumping .1. Theory." Journal of Applied Physics, **34**(2): 246-250.

Rada, M. (2004). "Electrohydrodynamic (EHD) pumping of liquid nitrogen-application to spot cryogenic cooling of sensors and detectors." Mechanical Engineering, College Park, University of Maryland.

Richter, A., and Sandmaier, H. (1990). "An electrohydrodynamic micropump." IEEE Micro Electro Mechanical Systems. An Investigation of Micro Structures, Sensors, Actuators, Machines and Robots, New York, NY, USA

Richter, A., Plettner, A., Hofmann, K.A., and Sandmaier, H. (1991). "A micromachined electrohydrodynamic (EHD) pump.", Sensors and Actuators, A 29: 159–168.

Singhal, V., and Garimella, S.V. (2005). "A Novel Valveless Micropump With Electrohydrodynamic Enhancement for High Heat Flux Cooling." IEEE Trans. ON ADVANCED PACKAGING, 28(2): 216-230.

Singhal, V., and Garimella, S.V. (2006). "Induction electrohydrodynamics micropump for high heat flux cooling." Sensors and Actuators A, Article In Press

Stratton, J. A. (1941). Electromagnetic theory. New York, London,, McGraw-Hill book company inc.

Stuetzer, O.M. (1959). "Ion drag pressure generation.", *J. Appl. Phys.*, 30(7): 984–994.

Stuetzer, O. M. (1960). "Ion Drag Pumps." Journal of Applied Physics, **31**(1): 136-146.

Tuckerman, D.B., and Pease, R.F.W. (1981). "High-performance heat sinking for VLSI.", IEEE Electron Dev. Lett., 2: 126–129.

Van Lintel, H.T.G., van De Pol, F.C.M., and Bouwstra, S. (1998). "A piezoelectric micropump based on micromachining of silicon." Sens. Actuators, **15:** 153–167.

Wawzyniak, M., Seyed-Yagoobi, J., and Morrison, G.L. (2000). "An experimental study of electrohydrodynamic induction pumping of a stratified liquid/vapor medium."ASME J. Heat Transfer, 122: 200–203.

Wong, C.C., Chu, D., Liu, S.L., Tuck, M.R., Mahmud, Z., and Ammatucci, V. (1997). "Rapid Prototyping of a Micro Pump for Microelectronic Applications." Sanidia national laboratory report, California, USA.

Yang, L.-J., and J.-M. Wang(2003). "The micro ion drag pump using indium-tin-oxide (ITO) electrodes." IEEE The 16th Annual International Conference on Micro Electro Mechanical Systems, Piscataway, NJ, USA.

Yazdani, M., and Seyed-Yagoobi, J. (2007). "Electrically Induced Dielectric Liquid Film Flow Based on Electric Conduction Phenomenon." J. Fluid Mechanics, article in press.

Appendix A
Manufacturing process

Electrodes fabrication process

Glass substrate cleaning

- Rinse with acetone for 15 seconds.

- Rinse with methanol for 15 seconds.

- Rise with de-ionized (DI) water for 5 minutes.

- Dry the sample using compressed nitrogen.

- Dehydrate the sample at 110°C for 2 min.

Metal deposition

- Deposit a 100 Å thick chromium layer.

- Deposit a 2400 Å thick gold layer.

Patterning pillars mould

- Plasma oxidize the substrate at 80 W for 1 min.

- Spin AZ P4620 for 30 sec at 500 rpm, ramp to 2000 rpm in 2 sec.

- Bake the sample at 95°C ramp to 120°C for 6 min.

- Expose the substrate using pillars' mould mask for 65 sec at 7.2 mJ/sec.

- Develop photoresist in 1:4 AZ 400K to DI water solution for 8 minutes.

- Rinse with DI water for 5 minutes.

- Dry with compressed nitrogen.

- Dehydrate the sample at 110°C for 2 min.

Electroplating nickel

- Plasma oxidize the sample at 80 W for 5 min.

- Mix ingredients presented in Table3.1 with DI water for electroplating solution.

- Submerge substrate and a nickel target in the electroplating solution.

- Stir the solution with magnetic stir bar and stirrer.

- Heat the solution and adjust the temperature at 50°C.

- Use a DC power supply. Connect cathode to substrate and anode to nickel target.

- Set the current density to 10 mA/cm^2.

- Remove the sample from the solution after 1:30 hr.

- Rinse the sample with DI water for 5 min.

- Rinse the sample with acetone until the photoresist is removed.

- Rinse the sample with methanol for 15 sec.

- Rinse with DI water for 5 min.

- Dry the substrate using compressed nitrogen.

- Dehydrate the sample at 110 for 2 min.

- Plasma oxidize the substrate at 80 W for 5 min in order to completely remove the photoresist residual.

Patterning the electrode base

- Spin S 1808 photoresist for 30 sec at 3000 rpm

- Bake the sample at 110°C for 90 seconds.

- Expose the substrate using electrode base mask for 6 sec at 7.2mJ/sec.

- Bake the sample at 130°C for 3 min.

- Develop photoresist in 1:4 developer 351 to DI water solution for 45 seconds.

- Rinse with DI water for 5 min.

- Dry with compressed nitrogen.

- Etch the gold with nickel compatible gold etchant for 1 min.

- Etch the chromium with nickel compatible chromium etchant for 2.5 min.

- Rinse with acetone to remove the photoresist.

- Rinse with methanol for 15 sec.

- Rinse with DI water for 5 min.

- Dehydrate the sample at 110°C for 2 min.

- Dice the sample into individual micropumps.

Microchannel fabrication

Silicon substrate cleaning

- Rinse with Acetone for 15 sec.

- Rinse with methanol for 15 seconds.

- Rise with de-ionized (DI) water for 5 min.

- Dry the sample using compressed nitrogen .

- Dehydrate the sample at 110°C for 2 min.

Patterning microchannel mould

- Plasma oxidize the substrate at 50 W for 1 min.

- Spin SU-8 100 for 30 sec at 3000 rpm.

- Bake the substrate at 65°C for 10 min and at 95 °C for 30 min.

- Expose the substrate using microchannel mould mask for 90 sec at 7.2 mJ/sec.

- Bake the substrate at 65°C for 1 min and at 95 °C for 10 min.

- Develop for 10 min in 1:3 SU-8 developer to DI water solution.

- Rinse with DI water for 5 min.

- Hard-bake the sample at 130°C for 5 min.

Casting PDMS micro channel

- Mix 15 ml of PDMS with 1.5 ml of curing agent.

- Degasify the mixture in dessicator for 5 min.

- Pour PDMS over microchannel mould and bake it at 65°C for 1 hour.

- Peel off PDMS from the silicon substrate.

- Cut each micro channel with 2 mm rim.

- Punch inlet and out let using glass micro-pipette.

Integrating PDMS microchannel on electrodes substrate.

- Solder cupper wires to electrode pads.

- Plasma oxidize the electrode substrate and PDMS microchannel at 50 W for 45 sec.

- Align the micro channel on substrate according to electrodes.

- Pre-heat the substrate and PDMS on heat plate at 150°C for 2 min.

- Mix 10 ml of PDMS with 0.5 ml of curing agent.

- Using a syringe with needle pour the PDMS mixture on the border of PDMS microchannel on glass substrate.

- Bake the sample for 3 min at 150°C.

- Plasma oxidize the micropump and glass tubings at 50 W for 45 sec.

- Implement glass tubings in inlet and outlet holes.

- Pre-heat the micropump with glass tubings on heat plate at 150°C for 2 min.

- Using a syringe with needle pour the PDMS mixture around glass tubing on the PDMS microchannel.

- Bake the sample for 3 min at 150°C.